


Article

Response of Cyclonic Eddies to Typhoon Surigae and Their Weakening Effect on the Kuroshio Current in the Western North Pacific Ocean

Yanzeng Zhang ¹  and Shuzong Han ^{1,2,*}

¹ College of Oceanic and Atmospheric Sciences, Ocean University of China, Qingdao 266100, China; yanzengzhang@stu.ouc.edu.cn

² Yazhou Bay Innovation Institute, Hainan Tropical Ocean University, Sanya 572025, China

* Correspondence: hansz@ouc.edu.cn

Abstract: This study investigated the dynamic and thermal responses of cyclonic eddies (CEs) to Typhoon Surigae in the western North Pacific Ocean using satellite data and a coupled ocean–atmosphere model. Observations and simulations revealed that the typhoon enhanced the two preexisting CEs (C1 and C2). After the typhoon passed the two eddies, the sea surface height (SSH) lowered and the eddy velocity increased above 200 m. C1 was stretched with elliptical deformation accompanied by an SSH trough and jets on the sides of the typhoon track at the eddy edge. The comparative experiments indicated that the typhoon caused the SSH of C1 and C2 to lower by 53.52% and 25.14% compared to conditions without the typhoon, respectively, and the kinetic energy of C1 and C2 to increase by 12 times and 65.76%, respectively. The positive vorticity anomaly input from the typhoon to the CEs was the main mechanism for the enhancement of the CEs. The enhanced CEs modulated the typhoon-induced sea surface temperature (SST) cooling, causing the temperature within the eddies to decrease by upwelling and mixing, and the SST cooling became significant at the center of the CEs and propagated westward with the eddies. This study also revealed that typhoons can significantly perturb eddy dynamic structures by enhancing or generating cyclonic cold eddies and eradicating anticyclonic eddies, thereby weakening the Kuroshio Current transport via eddy–Kuroshio interactions.



Citation: Zhang, Y.; Han, S. Response of Cyclonic Eddies to Typhoon Surigae and Their Weakening Effect on the Kuroshio Current in the Western North Pacific Ocean. *J. Mar. Sci. Eng.* **2024**, *12*, 1202. <https://doi.org/10.3390/jmse12071202>

Academic Editor: João Miguel Dias

Received: 14 June 2024

Revised: 9 July 2024

Accepted: 12 July 2024

Published: 17 July 2024



Copyright: © 2024 by the authors. Licensee MDPI, Basel, Switzerland. This article is an open access article distributed under the terms and conditions of the Creative Commons Attribution (CC BY) license (<https://creativecommons.org/licenses/by/4.0/>).

Keywords: oceanic cyclonic eddy; typhoon; Kuroshio; coupled ocean–atmosphere model; air–sea interaction; western North Pacific

1. Introduction

Tropical cyclones (TCs) are intense mesoscale weather phenomena that originate and intensify in tropical and subtropical regions. In the western North Pacific Ocean (WNPO), TCs with maximum wind speeds greater than $32.7 \text{ m}\cdot\text{s}^{-1}$ are known as typhoons. They play an important role in the local marine environment and in global ocean heat transport through momentum and heat exchange with the ocean [1–4]. The impact of typhoons on the upper ocean is a complex process involving multiscale dynamics, including large-scale circulation, mesoscale eddies, upwelling, near-inertial oscillations, and turbulent mixing [5]. Among these phenomena, mesoscale eddies are ubiquitous quasigeostrophic motions with spatial scales ranging from a few kilometers to hundreds of kilometers and temporal scales ranging from days to months; mesoscale eddies contribute more than 80% of ocean kinetic energy and are known as “storms in the ocean” [6]. They play an essential role in ocean heat and material transport, energy cascades, and in modulating large-scale circulation [7–9].

The WNPO has abundant eddies [10,11]. Moreover, it has been more significantly affected by increases in the frequency and intensification of TCs in recent decades [11,12]. Therefore, typhoon–eddy interactions are prevalent, and 90% of the typhoons in the WNPO pass through eddies during their movements [13]. The interactions between mesoscale

eddies and typhoons constitute a crucial aspect of the oceanic response and feedback to typhoons; in particular, cyclonic eddies (CEs) induce a negative feedback to TCs through enhanced sea surface temperature (SST) cooling caused by special cold-core structures, which is important for typhoon forecasting [13,14].

Typhoons can impact the dynamic structures of preexisting CEs. First, they can increase the amplitude and radius of the CEs, which is known as ‘enhancement’. Second, they may cause the horizontal shape of the CEs to transform from oval to circular [15]. This enhancement is mainly attributed to the geostrophic upwelling induced by the counter-clockwise winds of typhoons, and the ellipticization process depends on the shear exerted by the wind stress curl on the surface eddies [15]. A slow-moving typhoon also increases the kinetic energy and effective potential energy of CEs [16,17]. Additionally, typhoons can induce the generation of new cyclonic cold eddies, mainly related to the input of positive vorticity to the ocean due to typhoon cyclonic winds [14,16,18,19].

The mixing layer in CEs is shallow due to their relatively unstable thermal structure and upwelling, which can contribute to typhoon-induced SST cooling and strongly influence the upper ocean response [13,20–23]. Ma et al. [24] analyzed the interactions between TCs and mesoscale eddies in the WNPO and found that cold eddies increase the recovery time of SST, and the westward propagation of SST cooling during the recovery period may be caused by the westward propagation of cold eddies. The SST cooling by TCs combined with mesoscale eddies is characterized by a combination of upwelling, wind-driven mixing, and enhanced mixing driven by shear at the bottom of the mixed layer [25,26]. The importance of advection processes in cold eddy-modulated SST effects has been emphasized in a recent study [27]. The impact of typhoons on eddy structures is not only limited to the surface but may also cause anomalous signals in the cold-core (warm-core) structure of the upper layer of cyclonic eddies (anticyclonic eddies, AEs) to propagate to the deeper layers of the eddy, affecting the three-dimensional thermohaline structures of the eddy [28].

In a warming climate, enhanced typhoons in eastern Taiwan have increased the energy of CEs relative to that of AEs, which may lead to the strengthening of the Kuroshio Current [29]. In this feedback mechanism between TCs and climate warming, the response of CEs to typhoons may play a key role, which is significant for assessing the response and feedback of large-scale circulation to climate change. Notably, the impact of typhoons on large-scale circulation can also be significant [30]. Hence, the variations and dynamic adjustments of the three-dimensional structures of CEs under typhoon forcing and the impacts of CEs and typhoons on the Kuroshio Current in the subtropical western boundary current region of the WNPO need to be further investigated. With the development of numerical models, coupled ocean–atmosphere models have shown advantages in simulating the impact of typhoons on the ocean [31,32]. However, few studies have used coupled ocean–atmosphere model experiments to analyze eddy responses. In this study, we selected Typhoon Surigae in 2021 as a case study, investigated the dynamic evolution, thermal responses, and energy changes of underlying cyclonic eddies influenced by typhoons, and examined their impacts on the Kuroshio Current.

The remainder of this paper is organized as follows. Section 2 describes the observations, reanalysis data, coupled ocean–atmosphere model, and methods used in this study. Section 3 details the responses of the two oceanic cyclonic cold eddies to Typhoon Surigae from observations and numerical models. In addition, the long-term evolution of TC-enhanced eddies and their impact on the Kuroshio Current are explained. Section 4 offers the main conclusions, discusses the shortcomings, and provides recommendations for future research.

2. Materials and Methods

2.1. Information on Typhoon Surigae

Typhoon Surigae developed as a tropical storm at 18:00 UTC on 12 April 2021 in the WNPO and moved northwestward, gradually increasing in intensity (Figure 1). At 12:00 UTC on 17 April, Surigae reached its maximum intensity with a maximum central wind

speed of 170 knots and a central pressure of 882 hPa. According to the typhoon intensity category on the Saffir–Simpson Hurricane scale (SSHS), its intensity ranged from Category 1 to Category 5 in 24 h, indicating rapid intensification [33]. Then, it decreased in intensity to Category 4, slowly moved northward, and passed through two cyclonic eddies from 18 April to 22 April (Figure 1). At 06:00 UTC on 25 April, Surigae degenerated into an extratropical cyclone. Typhoon Surigae was the strongest tropical cyclone ever recorded in April, known as “the King of Wind in April”.

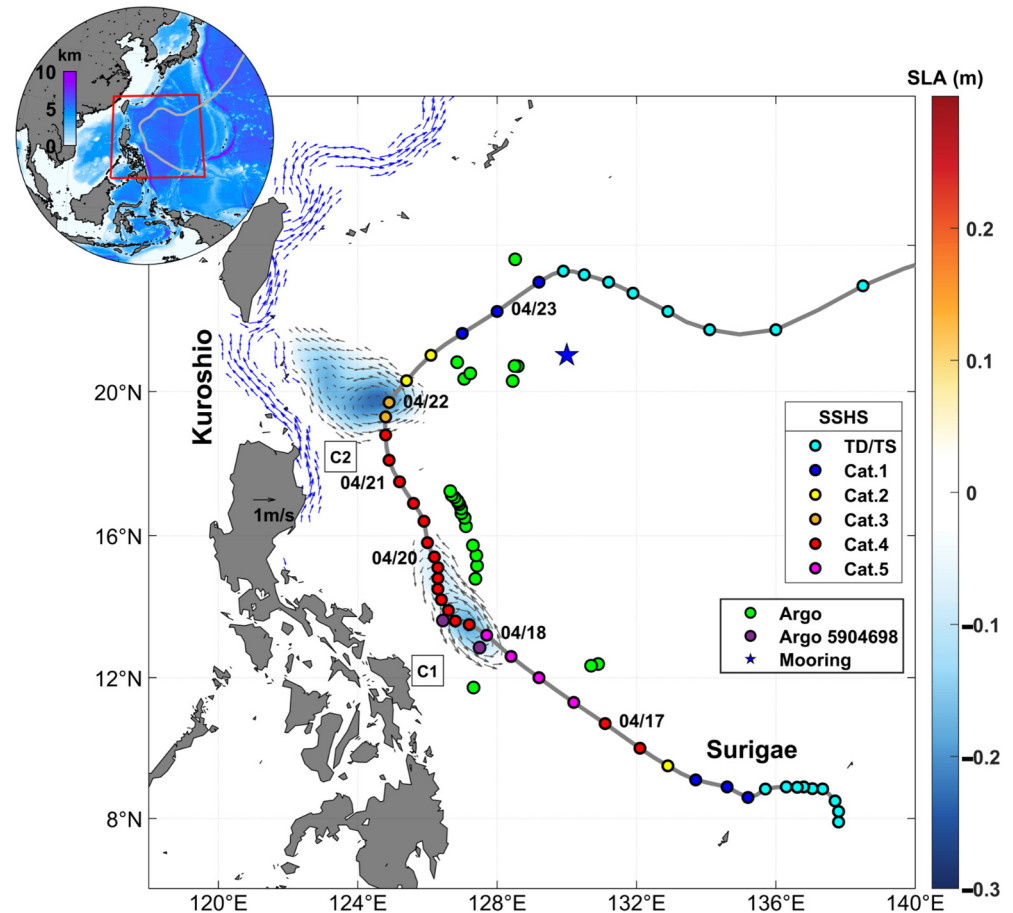


Figure 1. Tracks of Typhoon Surigae (displayed at 6 h intervals from IBTrACS) and the mean sea level anomaly (SLA) from 18 April to 23 April. The gray solid line indicates the track of Surigae, the colored dots represent the typhoon intensity category according to the Saffir–Simpson Hurricane scale (SSHS), and the date labels (month/day) indicate 00:00 UTC of the day. C1 and C2 are the two cyclonic cold eddies. The arrows indicate the geostrophic velocity vector, whereas the blue arrows denote the Kuroshio Current. The green dots are Argo floats within 200 km of the typhoon track from 16 April to 30 April, the purple dots are Argo 5904698, and the blue pentagram indicates mooring station M1.

Observations of Typhoon Surigae were provided by the International Best-Track Archive for Climate Stewardship (IBTrACS) version 4.0 provided by the National Oceanic and Atmospheric Administration (NOAA) [34]. The dataset includes information on the time, track, central air pressure, maximum wind speed, and speed of movement of tropical cyclones in Coordinated Universal Time (UTC) format, with a temporal resolution of 3 h. In addition, two typhoon tracks and central pressure data provided by the Tropical Cyclone Data Center of the China Meteorological Administration (CMA) and the Japan Meteorological Agency (JMA) were also used for comparison.

2.2. Observations

2.2.1. Satellite Observations

The sea level anomaly (SLA), sea surface height (SSH), and geostrophic velocity data used in the study are daily products (SEALEVEL_GLO_PHY_L4_MY_008_047) with a horizontal resolution of $0.25^\circ \times 0.25^\circ$ provided by the Copernicus European Marine Environmental Monitoring Service (CMEMS). This product has been widely used for the identification and analysis of mesoscale eddies in the WNPO [35–37].

The daily SST data are from the Operational Sea Surface Temperature and Ice Analysis (OSTIA) developed by the United Kingdom Meteorological Office (UKMO), which incorporates satellite remote sensing data as well as in situ data [38]. The horizontal resolution of the OSTIA is $0.05^\circ \times 0.05^\circ$; OSTIA SST data are also available from the CMEMS.

The sea surface wind data are from the Cross-Calibrated Multi-Platform (CCMP) grid production version 3.1 provided by Remote Sensing Systems (RSSs) [39]. The 10 m vector winds were mainly used for model validation and calculation of energy input from the typhoon. The horizontal resolution of the CCMP data is $0.25^\circ \times 0.25^\circ$, and the temporal resolution is 6 h.

2.2.2. Argo Floats and Moored Data

Several Argo floats operated near Surigae’s track, providing materials for assessing the accuracy of numerical simulations and analyzing the vertical thermal response of the ocean (Figure 1). The Argo thermohaline profiles are available from the EU Argo Center. In addition, we used temperature, salinity, and velocity data measured by conductivity–temperature–depth (CTD) instruments, temperature–depth (TD) instruments, and acoustic Doppler current profilers (ADCPs) from moorings for model validation. The details of the measurements from the mooring are shown in Table S1.

2.3. Reanalysis Datasets

To generate the initial and boundary conditions in the Regional Ocean Modeling System (ROMS) model, we used the reanalysis data from the Hybrid Coordinate Ocean Model (HYCOM) developed by the U.S. Naval Research Laboratory (NRL). The HYCOM reanalysis data provides three-dimensional ocean temperature, salinity, and horizontal currents with a horizontal resolution of $1/12^\circ$, which is at the level of eddy resolution. There are 40 vertical layers, and the temporal resolution is 3 h. This reanalysis data assimilates data from various observations, such as satellite altimeters, expendable bathythermography (XBT), CTD, and Argo floats. The National Centers for Environmental Prediction Final Analysis (NCEP FNL) global operational analysis data from the Global Data Assimilation System (GDAS) were used to create the initial and boundary conditions for the Weather Research and Forecasting (WRF) model in the coupled ocean–atmosphere model, with a horizontal resolution of $1^\circ \times 1^\circ$ and a temporal resolution of 6 h.

The features of the Kuroshio Current were confirmed by the $1/12^\circ$ ocean reanalysis datasets of the global ocean physics analysis and forecast system (GLOBAL_MULTIYEAR_PHY_001_030 and GLOBAL_ANALYSISFORECAST_PHY_001_024) distributed by the CMEMS. The CMEMS ocean reanalysis datasets with 50 vertical levels are based on the NEMO platform. The three-dimensional velocity data were used in this study to analyze the variation in the Kuroshio Current.

2.4. Typhoon Parameters

The wind stress τ and the typhoon-induced Ekman pumping velocity (EPV) are calculated as follows [1]:

$$\tau = \rho_a C_d / U_{10} / U_{10} \tag{1}$$

$$EPV = \frac{\nabla \times \tau}{\rho_w f} \tag{2}$$

where ρ_a is the air density, which is taken as a constant of $1.29 \text{ kg}\cdot\text{m}^{-3}$; \mathbf{U}_{10} is the 10 m wind vector (in $\text{m}\cdot\text{s}^{-1}$); ρ_w is the density of seawater, taken as a constant of $1024 \text{ kg}\cdot\text{m}^{-3}$; and f is the Coriolis parameter. C_d is the drag coefficient, which is defined according to [40]:

$$C_d = \begin{cases} (4 - 0.6|U_{10}|) \times 10^{-3} & |U_{10}| < 5 \text{ m/s} \\ (0.737 + 0.0525|U_{10}|) \times 10^{-3} & 5 \text{ m/s} \leq |U_{10}| < 25 \text{ m/s} \\ 2.05 \times 10^{-3} & |U_{10}| \geq 25 \text{ m/s} \end{cases} \quad (3)$$

The forcing time of a typhoon on the ocean is a parameter that combines the speed, intensity, and size of a typhoon’s translation, and can be used to explain the differences in the characteristics of cyclonic eddy physical parameters in response to different typhoon forcings [16]. The typhoon impact region is first defined as the area where the wind speed exceeds the critical wind speed ($U_c = 34$ knots) along the typhoon track, based on the typhoon track data and maximum wind speed radius at a 3 h resolution. Then, the total time that each grid is within the typhoon impact region during the entire typhoon impact period is calculated as the forcing time of the typhoon.

Typhoon wind stress affects the ocean and inputs energy to the upper ocean, causing changes in eddy kinetic energy. The energy input from the typhoon to the surface currents is calculated as follows:

$$W = \int |\tau_x u + \tau_y v| dt \quad (4)$$

where u and v are the ocean zonal and meridional geostrophic velocities, respectively, and τ_x and τ_y are the zonal and meridional wind stress components, respectively.

2.5. Eddy Identification, Dynamic, and Thermal Parameters

The relative position of mesoscale eddies to TCs is one of the more critical factors influencing the response of eddies [14,41]. To accurately analyze the SST, SLA, and kinetic energy responses in the eddy regions under the influence of typhoons, we need to accurately identify the eddy center and edge. We adopt the Winding-Angle (W-A) algorithm based on current vectors to identify eddies [42,43]. In the identification of CEs, the algorithm initially considers the local minima of SLA as potential eddy centers. Then, streamlines are calculated and clustered based on geostrophic velocity anomalies. Finally, the outermost closed streamlines from the eddy centers are utilized as the eddy edges. Based on the SLA and geostrophic velocity anomaly data, two preexisting cyclonic eddies (C1 and C2) in the track of the typhoon were detected (Figure 1).

To analyze the dynamic process of CEs under the influence of typhoons, we calculated several dynamic parameters. The eddy kinetic energy (EKE) reflects the magnitude of the kinetic energy of the mesoscale eddy and is calculated as follows:

$$EKE = \frac{u^2 + v^2}{2} \quad (5)$$

The Rossby number (Ro) is a dimensionless measure of the relative importance of local non-geostrophic motions versus large-scale geostrophic motions. A larger Ro indicates a stronger local non-geostrophic effect and is defined as follows:

$$Ro = \frac{\zeta}{f} \quad (6)$$

where ζ is the vertical relative vorticity and $\zeta = \frac{\partial v}{\partial x} - \frac{\partial u}{\partial y}$.

The horizontal elongation (σ) of the eddy reflects the deformation characteristics and is calculated from the shear and tensile strain rates:

$$\sigma = \sqrt{\left(\frac{\partial v}{\partial x} + \frac{\partial u}{\partial y}\right)^2 + \left(\frac{\partial u}{\partial x} - \frac{\partial v}{\partial y}\right)^2} \quad (7)$$

In all the formulas, u and v are the zonal and meridional components of the geostrophic velocity, respectively.

To investigate the thermal response of the eddies, the ocean heat content (OHC) is calculated by integrating the temperature over depth [44]:

$$OHC = \rho_0 C_{pw} \int_{200}^0 T(z) dz \quad (8)$$

where ρ_0 is the density of seawater, C_{pw} is the specific heat of seawater, $\rho_0 C_{pw} = 4.0 \text{ MJ} \cdot \text{C}^{-1} \cdot \text{m}^{-3}$, T is the temperature, and the depth of integration is 0–200 m.

The vertical component of potential vorticity (PV) is a parameter that combines the dynamic and thermal characteristics of an eddy and is calculated as follows:

$$PV = -\frac{f + \zeta}{\rho} \frac{\partial \rho}{\partial z} \quad (9)$$

where ρ is the potential density.

In addition, the buoyancy frequency N^2 is a measure of seawater stability. When $N^2 < 0$, the water body is in an unstable state. Larger N^2 indicates weaker oceanic mixing and stronger stratification:

$$N^2 = -\frac{g}{\rho} \frac{d\rho}{dz} \quad (10)$$

2.6. Volume Transport of the Kuroshio Current

The volume transport (VT) of the Kuroshio Current in this study can be obtained by integrating the meridional velocity. The VT is calculated as follows:

$$VT = \int_{x_2}^{x_1} \int_{500}^0 V dz dx \quad (11)$$

where V is the meridional velocity, x_1 and x_2 are the east–west endpoints of the zonal sections, respectively. The depth of vertical integration is 0–500 m.

2.7. Coupled Ocean–Atmosphere Model

2.7.1. Configuration of the Coupled Model

To analyze the characteristics and mechanisms of typhoon impacts on eddies, we conducted numerical simulations using the Coupled Ocean–Atmosphere–Waves–Sediment Transport (COAWST) model system. The COAWST (version 3.7) model system used in the study consists of the WRF model (version 4.4.2) and the ROMS model (version 3.9), where the coupler is the Model Coupling Toolkit (MCT) version 2.6.0 [45].

The ROMS model operates on a rectangular orthogonal grid with a horizontal resolution of 9 km and 40 vertical sigma levels and is capable of resolving oceanic mesoscale processes. The turbulence closure scheme is a Generic Mixed Length-Scale (GLS03) turbulence closure scheme. The topography in the ROMS model is derived from ETOPO1. The horizontal resolution of the WRF model is 9 km, and thirty-four vertical levels are employed. The cumulus parameterization used in the WRF model is the Kain–Fritsch scheme [46]. The Purdue Lin scheme is chosen as the microphysics scheme [47]. The boundary layer scheme is the Yonsei University (YSU) scheme [48], and the land surface scheme is the unified Noah [49]. The shortwave and longwave radiation schemes are the Dudhia and RRTM schemes, respectively [50,51].

2.7.2. Design of the Numerical Experiments

To compare the differences and mechanisms of eddy evolution with and without typhoon forcings, we designed two numerical experiments. Both experiments have the same initial ocean conditions, with the main difference being the different atmospheric

forcing conditions. In the simulation reconstructing the process of TC–eddy interaction (EXP-TC), the initial and boundary conditions are constructed using FNL data. In the simulation without TC forcing (EXP-NoTC), to filter out the cyclonic wind signals of the typhoon, the variables of the FNL data are smoothed using a spatial 10-point running average before constructing the initial and boundary conditions of the WRF model. The main settings of the numerical simulation are shown in Table 1. The COAWST model was initialized to start at 00:00 UTC on 13 April 2021, and the results from the model output after 00:00 UTC on 16 April were selected for subsequent analyses to ensure that the ocean and atmosphere models achieved their spin-up time.

Table 1. Design of the numerical experiments in COAWST.

Configuration	EXP-TC	EXP-NoTC
ROMS model initial conditions	HYCOM (00:00 UTC 13 April 2021)	
WRF model initial conditions	Original FNL (00:00 UTC 13 April 2021)	Smoothed FNL (00:00 UTC 13 April 2021)
Simulation time	00:00 UTC 13 April 2021–00:00 UTC 01 May 2021	
Simulation area	118°–138° E, 8°–26° N	

EXP-TC reproduced the typhoon process with a positive wind stress curl at the center of the typhoon (Figure S1a–d). No typhoons formed in EXP-NoTC according to a comparative simulation (Figure S1e–h). Using these two numerical experiments, we can explore the mechanisms and contributions by which typhoons affect eddies.

3. Results and Discussion

3.1. Responses of the Two CEs to Surigae from Satellites and Argo Floats

3.1.1. SLA and Eddy Dynamic Parameters

Figure 2 shows the variation in the SLA of the CEs under the influence of Typhoon Surigae. Before Surigae, cold eddy C2 existed east of the Luzon Strait on 17 April, while the C1 eddy dynamic structure was weak and not identified by the W-A algorithm (Figure 2a). After Surigae passed through C1, C1 rapidly intensified, and the sea surface was lowered (Figure 2c,d). After Surigae passed C2, the sea surface of C2 was lowered, the eddy area increased, and the shape became more circular (Figure 2e–h). After the passage of Surigae, the two cold eddies propagated westward, and a new cyclonic eddy developed (Figure 2i–k). The new eddy was initially identified on 26 April (Figure 3d). Its shape stretched in the northwest-southeast direction, forming a flattened ellipse (Figure 3l). The generation of the new eddy may be related to barotropic instability due to the strong horizontal shear of the current induced by the typhoon (Figure 3d).

Using the grid-based maximum response (GMR) method developed by Li et al. [52] to calculate the typhoon-induced variation in the SLA, the sea surface can be lowered as much as 0.4 m according to Figure 2l. The lowered area was mainly concentrated on the left side of the typhoon track, resulting from the combined effect of the dynamic evolution of the eddy under the influence of the typhoon and its western propagation (Figure 2l). The sea surface height was significantly lowered in the C1 region because C1 did not have an obvious signal of negative SLAs before Surigae, and Surigae moved more slowly and with greater intensity during the stage of influencing C1 (Figure 1). For C2, the SLA changes were smaller than those for C1 because C2 was already stronger before Surigae, the relative distance between the centers of Surigae and C2 was greater than that of C1, and Surigae moved faster and was less intense while passing C2. A decrease in the sea surface height of cold eddies caused by typhoons has been revealed in a previous study [30]. In our study, the effect of Surigae on the sea surface height anomaly was similar. Following its passage through C1, a sea surface “trough” was induced in the typhoon’s track, which is similar to the “cold wake” after passing through C1, and propagated westward with the eddy

(Figure 2m). The SLA of C2 was also characterized by westward propagation, with a slight sea surface depression after the typhoon disturbance (Figure 2n).

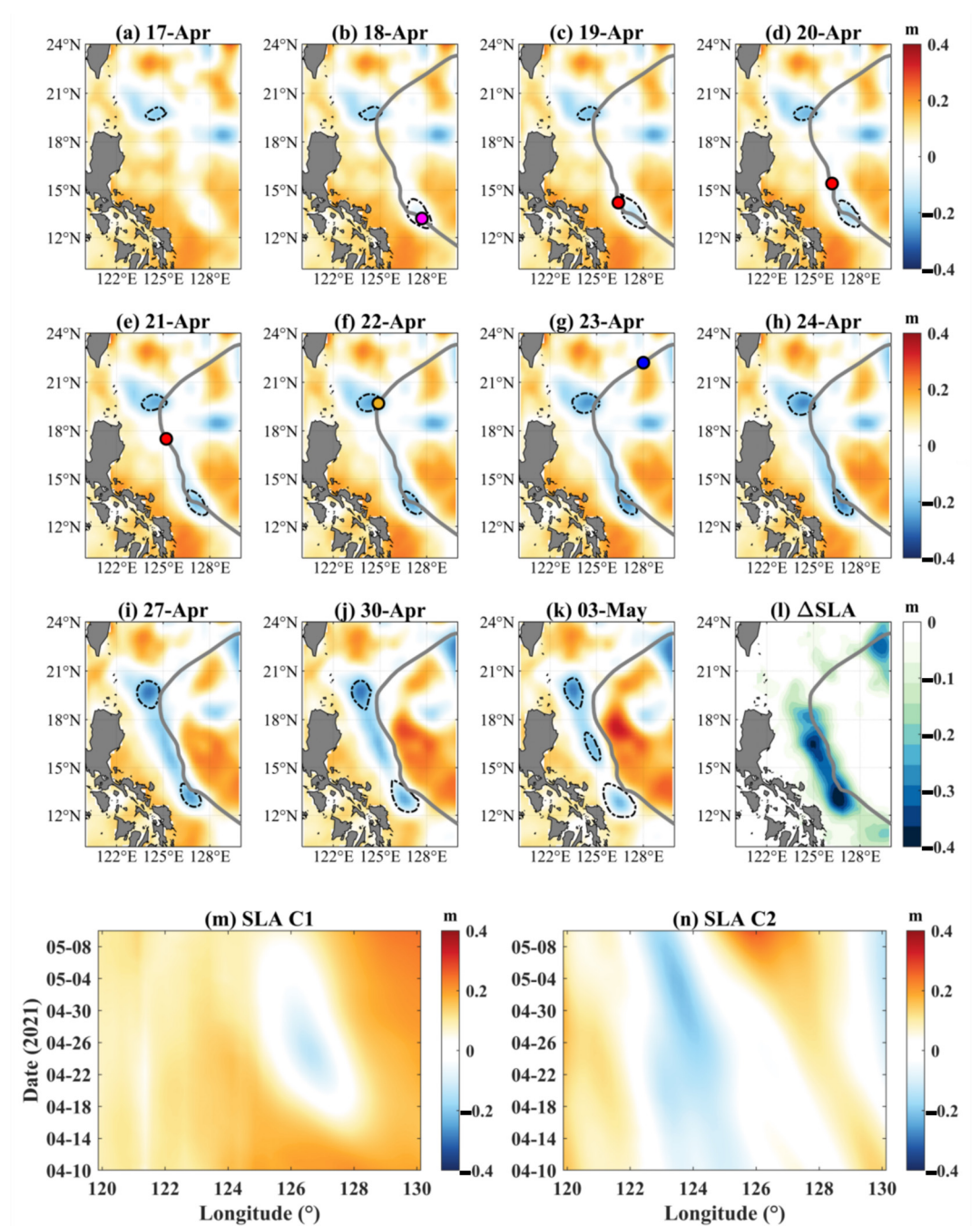


Figure 2. (a–k) Distributions of SLA before, during, and after Surigae, and (l) the typhoon-induced SLA reduction. The solid gray lines indicate the typhoon tracks, the black dashed lines indicate the edges of the identified cyclonic eddies, and the colored dots indicate the position of Surigae at 00:00 UTC on that day and the typhoon intensity. (m,n) Meridional average SLA between 10 April and 10 May for C1 and C2.

Compared with the conditions before the passage of the typhoon, C1 increased in EKE after being disturbed by the typhoon, and high-value areas appeared on both sides of the typhoon track (Figure 3a–d). The EKE of C1 reached a maximum of $0.73 \text{ m}^2 \cdot \text{s}^{-2}$ on 23 April, a maximum of $0.76 \text{ m}^2 \cdot \text{s}^{-2}$ on the 8th day after the passage of the typhoon, and a maximum of $0.86 \text{ m}^2 \cdot \text{s}^{-2}$ during the typhoon’s impacts. C2 did not show a significant

increase in EKE after the typhoon, but the velocity increased at the western edge of the eddy, with a maximum EKE of $0.25 \text{ m}^2 \cdot \text{s}^{-2}$.

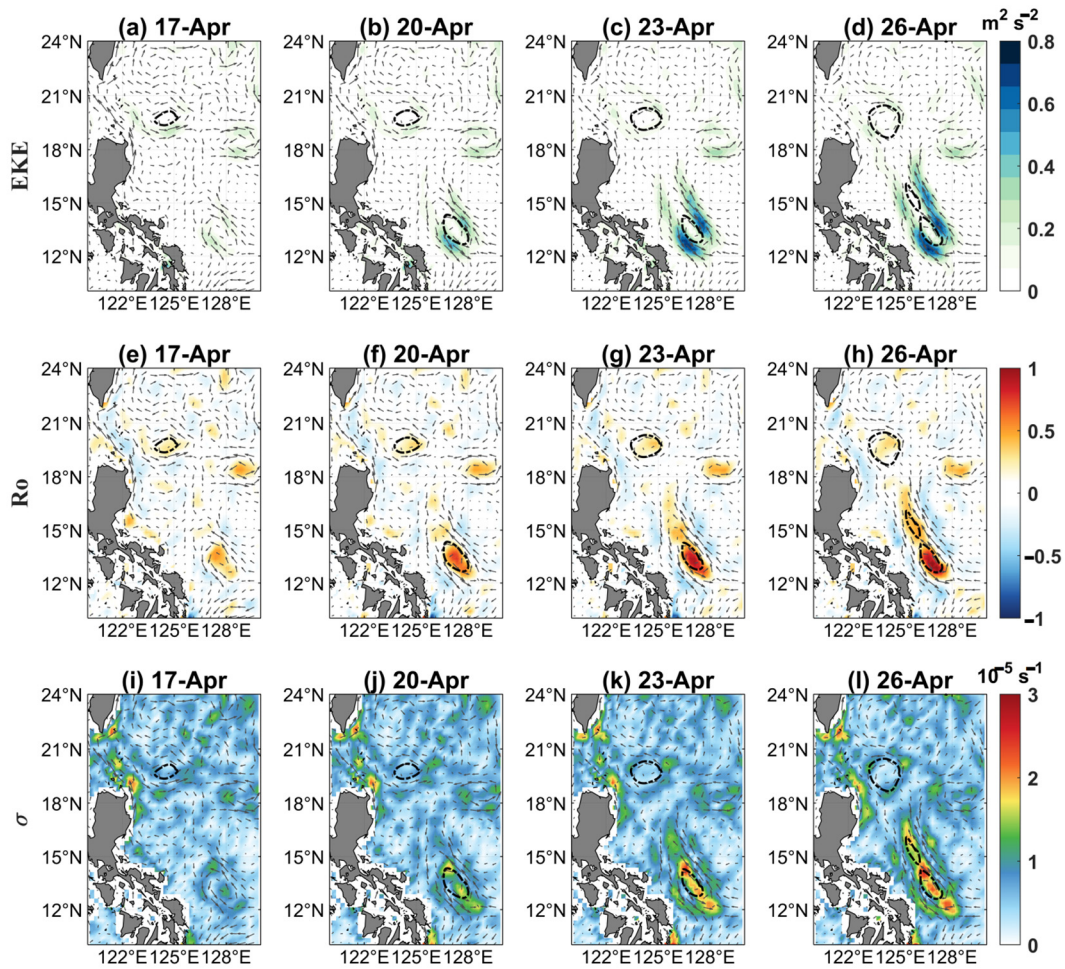


Figure 3. Distributions of (a–d) eddy kinetic energy (EKE), (e–h) R_o , and (i–l) σ before, during, and after Surigae. Arrows indicate geostrophic velocity vectors and black dashed lines indicate identified cyclonic eddy edges.

Before the passage of the typhoon, the centers of C1 and C2 were both areas with positive R_o values, with R_o values less than 0.5. After the passage of the typhoon, R_o increased in C1, reaching a maximum of 0.77 on 20 April and a maximum of 1.07 on 26 April, indicating an increase in the local non-geostrophic effect after the typhoon (Figure 3e–h). R_o in C2 reached a maximum of 0.42 on 23 April after the typhoon’s passage, and the range of positive vorticity expanded as the eddy area increased, but the lower R_o suggests that the submesoscale process may have been weaker than that in the C1 region.

The typhoon effect resulted in the enhancement of C1 and significant changes in its morphology. Under the action of the cyclonic wind of the typhoon, the cyclonic current was first stimulated at the sea surface, and due to the northwest-southeast direction of the typhoon, the flow field was also characterized by a strong jet in the northwest-southeast direction. C1 stretched in the northwest-southeast direction and compressed in the northeast-southwest direction, and the eddy exhibited elliptical features (Figure 3j,k). The horizontal deformation rate in region C1 reached $2.68 \times 10^{-5} \text{ s}^{-1}$, which was double that before the typhoon’s passage (Figure 3l). For C2, the shape underwent the process of ellipticization and then regularization, and the change in the eddy deformation rate was smaller (Figure 3i–l).

3.1.2. SST and Mixed Layer Temperature

Typhoon Surigae passed over C1 on 18 and 19 April, at which time C1 did not exhibit significant cold eddy structural features (Figure 4b,c). After the passage of the typhoon, significant cooling occurred in the C1 region, and the cooling area on the right side of the typhoon track was larger than that on the left side (Figure 4d,e). Prior to the typhoon’s passage, the cyclonic eddy present in the C2 region resulted in a cooler SST through the action of eddy upwelling (Figure 4a). After the typhoon passed through C2 on 22 April, a cold spot structure appeared in C2 (Figure 4g,h). By 30 April, the SST basically returned to the state before the typhoon’s impact, after which a cold core was present in the C2 region (Figure 4j,k).

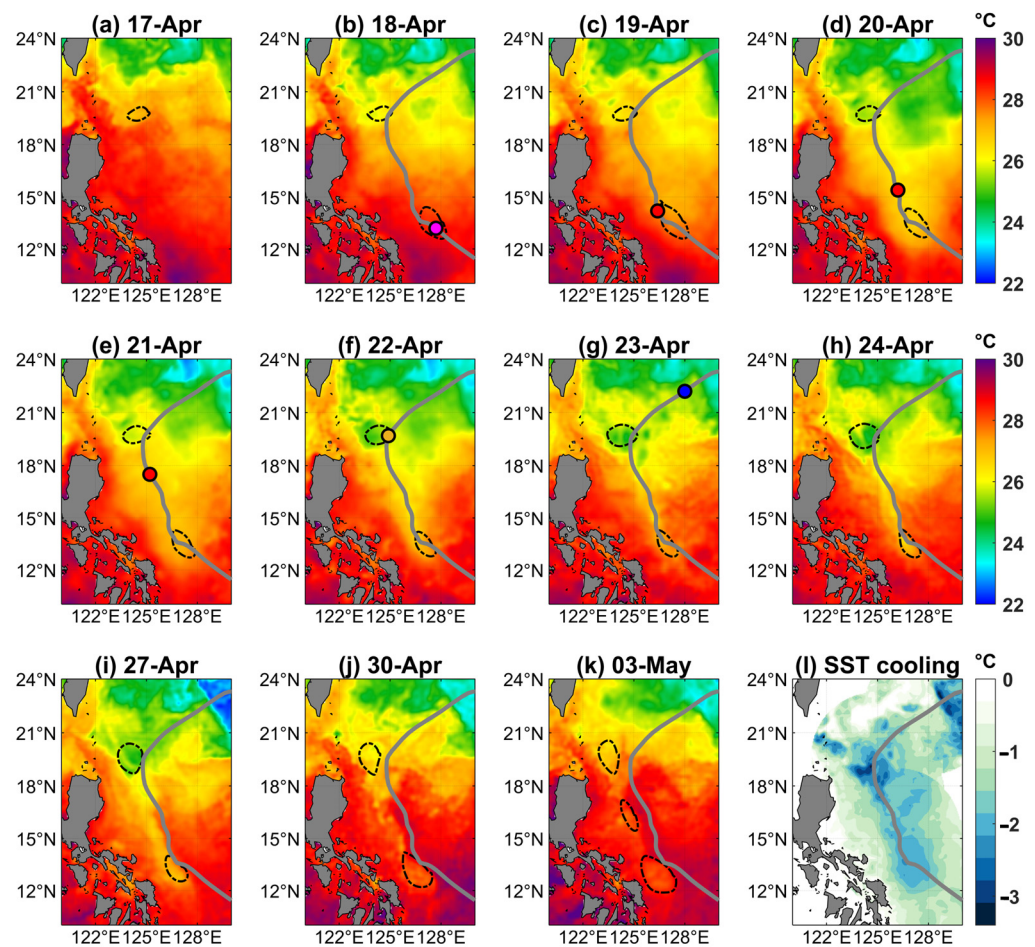


Figure 4. (a–k) Distributions of the sea surface temperature (SST) before, during, and after Surigae and (l) the SST cooling. The solid gray lines indicate the typhoon track, the black dashed lines are the edges of the identified cyclonic eddies, and the colored dots indicate the position of Surigae at 00:00 UTC on that day and the typhoon intensity.

In the process of SST cooling and recovery from warming, the cold eddies had a modulating effect on the SST. More intense cooling occurred in the eddy region, reaching a maximum of 3.4 °C. The recovery time was prolonged, and low-temperature features were still observed 7 days after the typhoon transited the region (Figure 4l). The modulation by eddies is consistent with the results of previous studies [22,35]. The cold area induced by the typhoon propagated westward during the recovery phase (Figure 4i), which may be related to the westward propagation of cold eddies [24].

The mixed layer depth (MLD) and mixed layer temperature (MLT) before and after the passage of the typhoon are calculated with the threshold method proposed by de Boyer Montégut et al. [53]. The water depth where the difference between the potential

density and the surface potential density exceeds $0.125 \text{ kg}\cdot\text{m}^{-3}$ is regarded as the MLD, and the mean temperature above the MLD is defined as the MLT. Argo float 5904698 (WMO ID number) was located at the edge of C1 (127.497° E , 12.851° N) on 16 April, when the typhoon had not yet passed through and the eddy structure of C1 was weak (Figure 1). On 26 April, float 5904698 moved inside C1, which had already strengthened due to the typhoon (Figure 3d). The MLD decreased from 46.87 m on 16 April to 13.35 m on 26 April, and the MLT decreased by 2.25° C . This indicates that the mixed layer was thicker before the passage of the typhoon, but the cyclonic cold eddy enhanced by the typhoon led to the upwelling of cold water, the temperature of the mixed layer decreased, and the depth of the mixed layer was reduced by the modulation of the cold eddy.

3.2. Three-Dimensional Responses of the Two CEs to Surigae in Numerical Experiments

3.2.1. Model Validation

The simulations of typhoon tracks and intensities mainly determine the accuracy of the simulations of upper ocean–atmosphere interactions. The simulated typhoon tracks of the COAWST EXP-TC experiment were examined using the typhoon best tracks from IBTrACS, CMA, and JMA, and it was found that the simulated tracks of the typhoon were basically in agreement with the results of the observations, and the deviation was less than 50 km (Figure 5a). Compared with those of the CCMP wind data, the wind speeds simulated by COAWST were greater in the early stage of the typhoon, but their trends were basically similar (Figure 5b). The trend of air pressure at the center of the typhoon simulated by COAWST was consistent with that of the measured data, with a maximum difference of 30 hPa from that of the measured data (Figure 5c). Overall, the results of the typhoon simulation by COAWST were deemed reliable, and the simulation results can be used to study the impacts of Typhoon Surigae on the upper ocean.

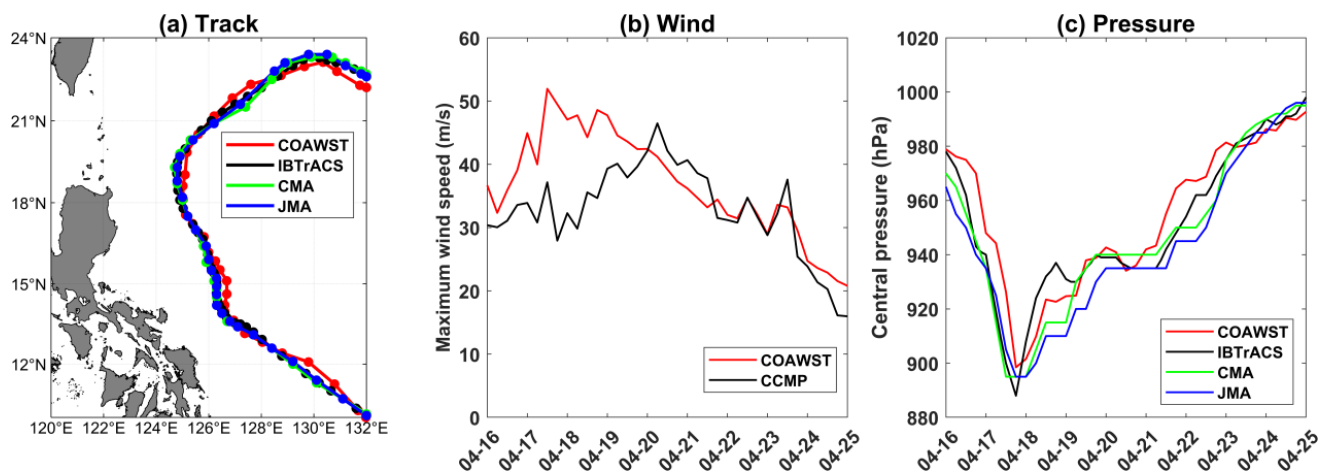


Figure 5. Comparisons of the (a) tracks, (b) maximum wind speeds at 10 m, and (c) central air pressure of Surigae between the observations and the EXP-TC results.

The location, shape, and SSH of the two eddies were well modeled by EXP-TC (Figure 6a,b). Both model simulations and satellite observations consistently showed that the EKE of C1 and C2 increased during the typhoon passage, and the model-simulated EKE was greater, indicating that the simulated upper-level current was stronger (Figure 6c). Numerical simulations also showed SSH depressions due to typhoons, which is consistent with satellite observations (Figure 6d).

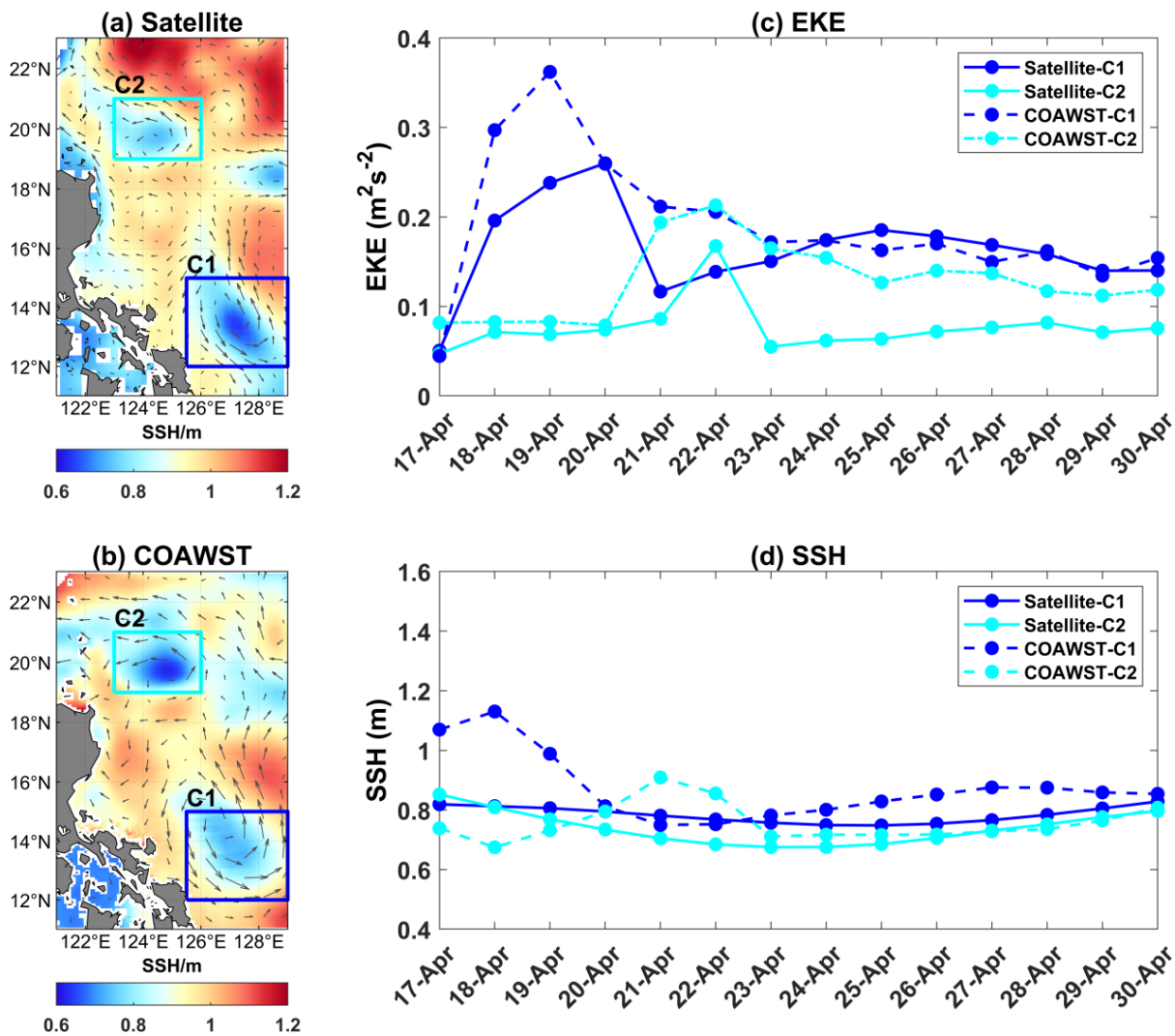


Figure 6. Distributions of the mean sea surface height (SSH) and surface velocity from 17 April to 30 April based on (a) satellite observations and (b) the EXP-TC simulation and variations in (c) the mean EKE and (d) the mean SSH in C1 and C2 from 17 April to 30 April.

The COAWST EXP-TC simulation results were further examined using the Argo profile data in Figure 1, the temperature data, and the velocity data observed by mooring M1. A linear fit of the simulated values to the observed values reveals that the correlation coefficient between the model-simulated and Argo-observed temperatures is 0.9759, and the correlation coefficient with the submerged marker observations is greater than 0.96, with a root mean square error (RMSE) of only 0.7683 °C (Figure 7a–c), indicating that the COAWST simulation of temperature is reliable. There is some bias in the simulated salinity. The correlation coefficient between the simulated salinity and the observed salinity is 0.8972, and the RMSE is 0.0698 psu (Figure 7b). The correlation coefficient between the simulated velocity and observation was 0.657, with an RMSE of 9.214 cm·s⁻¹, and the linear fit curve indicated a bias in the model-simulated velocity (Figure 7d). We are more concerned with the amount of variation in the upper ocean caused by Typhoon Surigae using numerical comparison experiments, so the bias in the salinity and current velocity of the simulations is acceptable and does not affect the relevant qualitative conclusions.

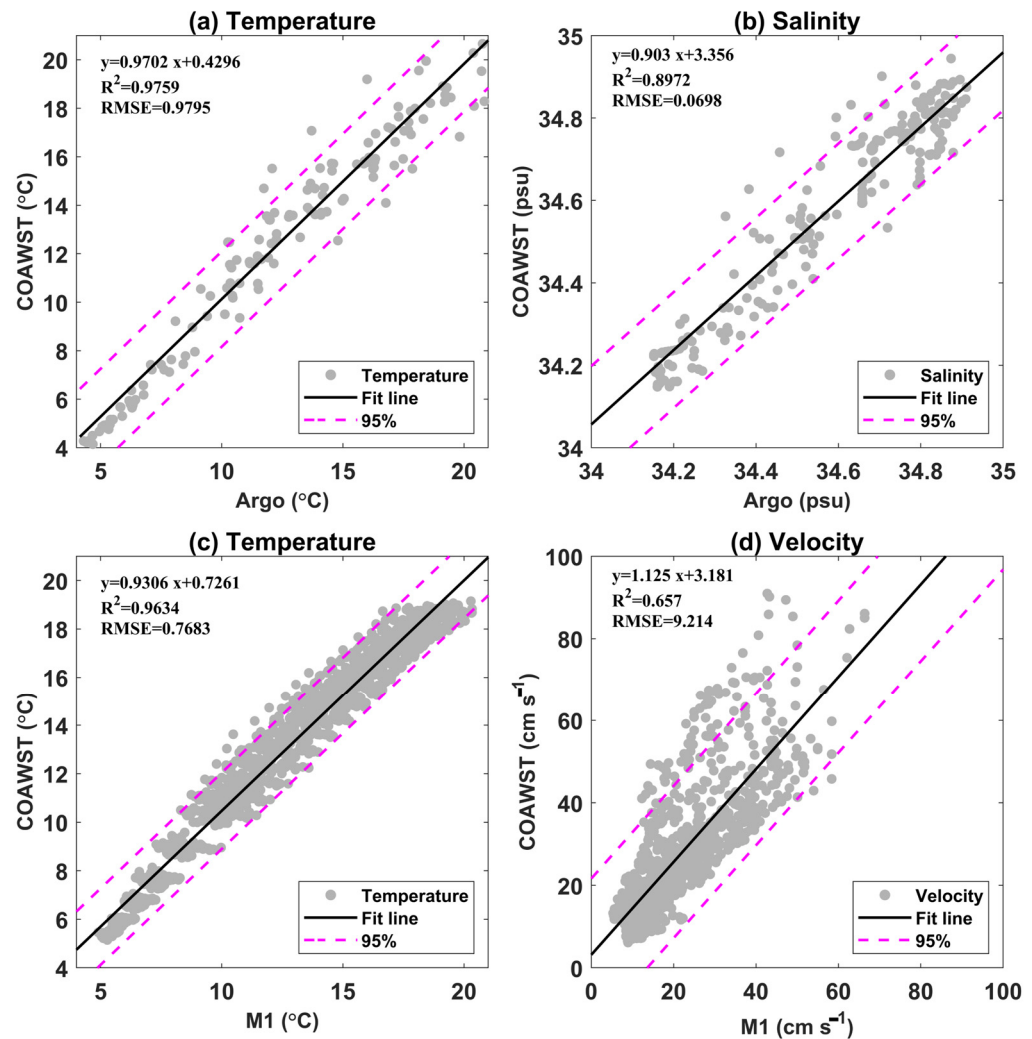


Figure 7. Comparisons of (a) temperature from Argo, (b) salinity from Argo, (c) temperature from M1, and (d) velocity from M1 with the EXP-TC simulation. The black solid lines indicate the regression line, and the magenta dashed lines are the 95% confidence intervals. In the regression equation, y is the model result, and x is the corresponding measured result. R^2 is the correlation coefficient between the model result and the measured result, and RMSE is the root mean square error.

3.2.2. Three-Dimensional Structural Response of Two Eddies

The EXP-TC reconstructed the interaction between the typhoon and the eddy, where the surface current exhibited cyclonic flow under the action of the cyclonic wind of the typhoon (Figure 8a). After the typhoon passed through C1, the SSH was lowered, and C1 gradually strengthened and increased in area, which is consistent with satellite observations (Figures 2b,c and 8b,d). C1 experienced tensile deformation with an elliptical shape along the typhoon track, which was attributed to the upwelling induced by the along-track typhoon [41]. The model simulations also showed enhanced upwelling in the eddy. Before the typhoon (18 April), the C1 center was not characterized by low temperatures. After the passage of the typhoon, the 20 °C isotherm was lifted approximately 75 m. Due to the increase in upwelling in the center of C1 and the increase in bottom cold water, the temperature difference between the center and the edge of C1 reached 2 °C, and this low-temperature anomaly was strongest above 300 m (Figure 8e–h). At the beginning of the typhoon affecting C1, the cyclonic current was mainly concentrated above 100 m. After the typhoon, with the adjustment of C1, the velocity increased, the depth of influence of the intense current increased to 300 m, and the eddy kinetic energy increased (Figures 3b,c and 8i–l).

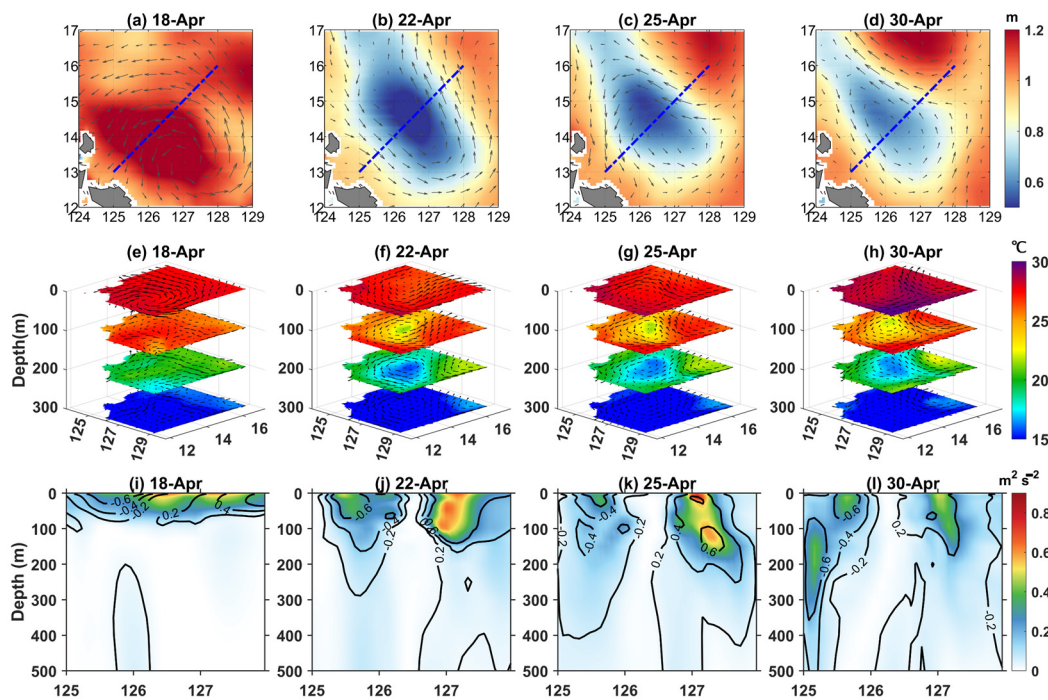


Figure 8. Distributions of the SSH and surface velocity of C1 for the EXP-TC simulation (daily averaged over 6 h time-resolved output results) on (a) 18 April, (b) 22 April, (c) 25 April, and (d) 30 April; (e–h) evolution of the 3D potential temperature and velocity; (i–l) distributions of the EKE above 500 m for the sections shown by the blue dashed lines, and the black solid lines are the contours of meridional velocity ($\text{m}\cdot\text{s}^{-1}$) at the same times as (a–d).

EXP-NoTC was used as a comparison experiment to simulate ocean eddies when there was no typhoon influence. Without typhoon forcing, the response of the upper ocean is quite different (Figure 9). C1 disappeared, and the cyclonic eddy structure was no longer present (Figure 9e–h), suggesting that typhoon forcing was responsible for the development of the otherwise weak C1.

Before the passage of the typhoon, an anticyclonic eddy existed on the southern side of C2 (Figure 9a). The cyclonic current was excited in the upper ocean during the typhoon, the anticyclonic eddy disappeared after the typhoon, and C2 strengthened (Figure 10a–d). The increase in C2 was accompanied by a decrease in the central SST (Figure 10e–h), mainly due to the increase in upwelling, and the $20\text{ }^{\circ}\text{C}$ isotherm lifted by approximately 50 m. The typhoon enhanced the velocity of C2, and the depth of influence of the intense current exceeded 400 m (Figure 10i–l). With the increase in C2, the meridional current exceeded $0.6\text{ m}\cdot\text{s}^{-1}$, and the EKE above 100 m on the eastern edge of the eddy exceeded $0.8\text{ m}^{-2}\cdot\text{s}^{-2}$ by 30 April (Figure 10l).

In EXP-NoTC, the anticyclonic eddy originally located to the south of C2 gradually strengthened, and a dipole eddy pair consisting of C2 and the anticyclonic eddy developed (Figure 9f–h). The anticyclonic eddy was enhanced, and the area of C2 decreased due to eddy–eddy interactions (Figure 11a–d). The core of C2 maintained a cold structure without significant cooling (Figure 11e–h). The EKE of C2 first increased, allowing the eddy to increase its depth of influence to 200 m. As the anticyclonic eddy strengthened, the EKE of C2 decreased (Figure 11i–l). Typhoons can cause anticyclonic eddies (generally warm eddies) to die after vorticity adjustment by inputting positive vorticity [54]. The comparative experiments conducted in this study revealed that strong typhoon winds can cause anticyclonic eddies to disappear and cyclonic eddies to strengthen and possibly prolong their life cycle, significantly affecting eddy features in the upper ocean.

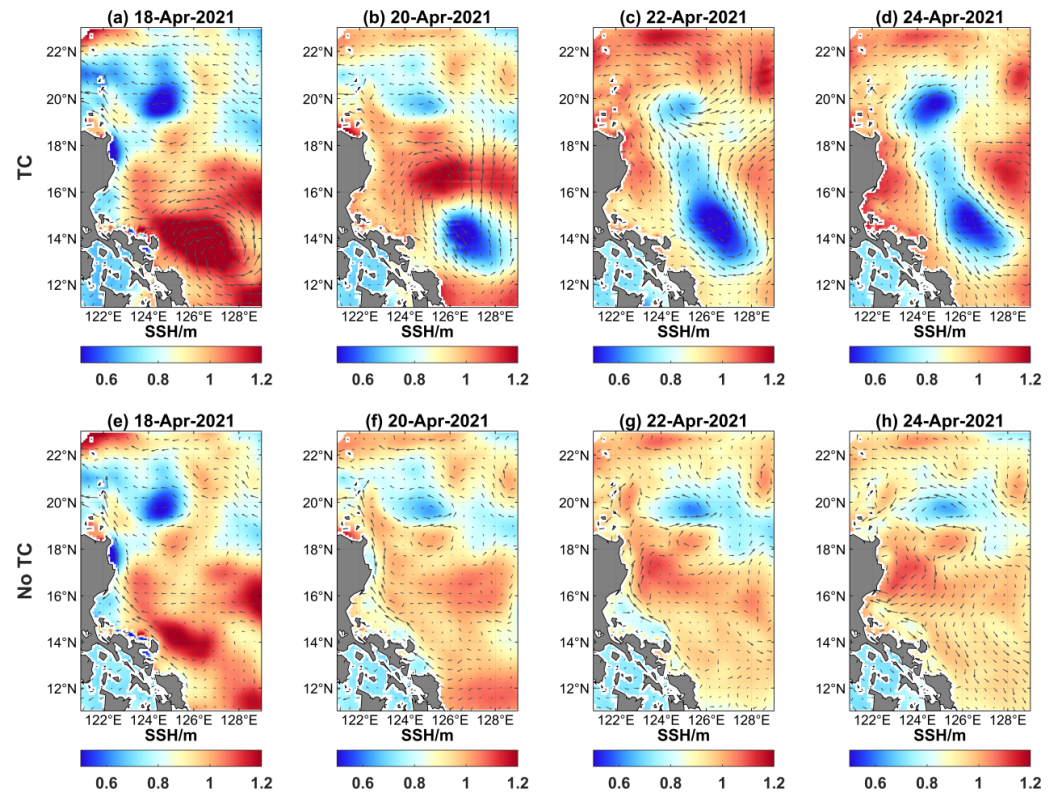


Figure 9. SSH and surface velocity (daily averaged) simulated by (a–d) EXP-TC and (e–h) EXP-NoTC.

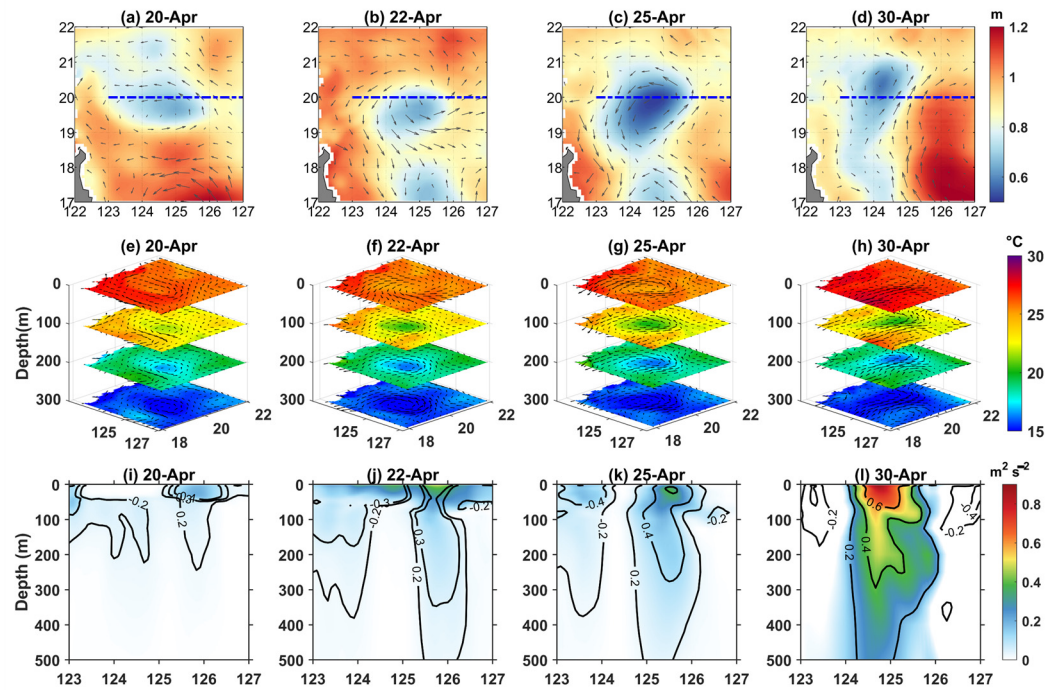


Figure 10. Distributions of the SSH and surface velocity of C2 for the EXP-TC simulation (daily averaged over 6 h time-resolved output results) on (a) 20 April, (b) 22 April, (c) 25 April, and (d) 30 April; (e–h) evolution of the 3D potential temperature and velocity; (i–l) distributions of the EKE above 500 m for the sections shown by the blue dashed lines, and the black solid lines are the contours of meridional velocity ($\text{m}\cdot\text{s}^{-1}$) at the same times as (a–d).

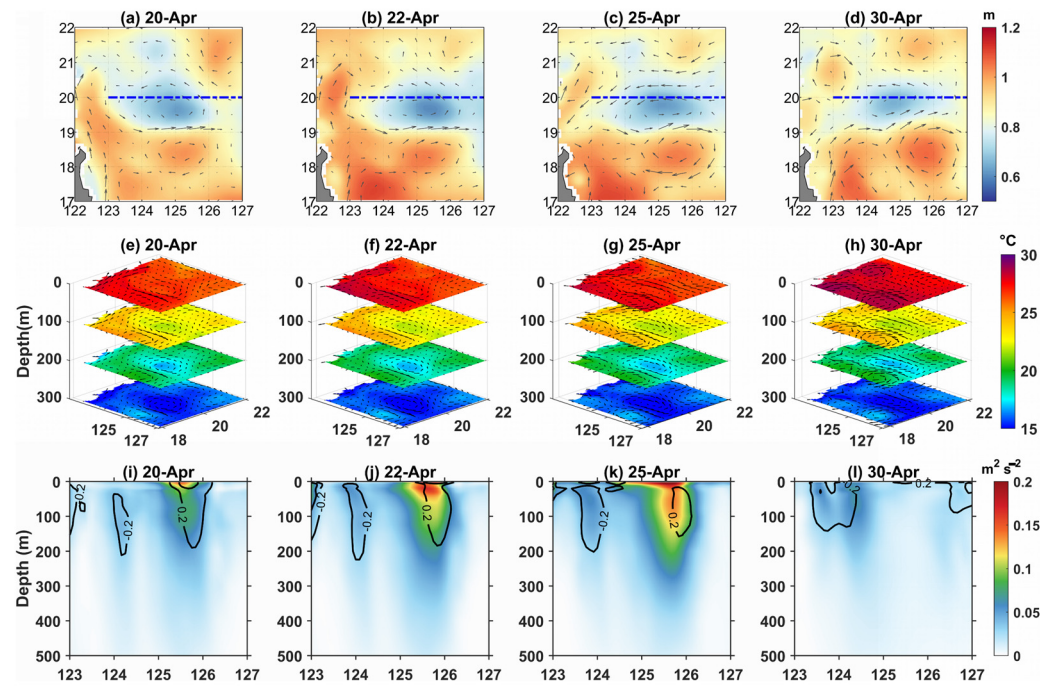


Figure 11. Distributions of the SSH and surface velocity of C2 for the EXP-NoTC simulation (daily averaged over 6 h time-resolved output results) on (a) 20 April, (b) 22 April, (c) 25 April, and (d) 30 April; (e–h) evolution of the 3D potential temperature and velocity; (i–l) distributions of the EKE above 500 m for the sections shown by the blue dashed lines, and the black solid lines are the contours of meridional velocity ($\text{m}\cdot\text{s}^{-1}$) at the same times as (a–d).

Notably, the response of the cyclonic eddy current to the typhoon was asymmetric, which corresponded to the deformation of the eddy. The strong velocity was related not only to the typhoon wind speed and direction but also to the direction of the typhoon track. The typhoon moved slowly to the northwest as it passed through C1, resulting in southward and northward jets on the left and right sides of the track, respectively, and the jet was stronger on the right side of the typhoon track (Figures 3b–d and 8i–k). As the typhoon passed C2, the winds weakened, a turning of the track occurred, and no jet was generated; rather, a counterclockwise current was further stimulated on the cyclonic eddy, and the velocity increased near the center of the typhoon (Figure 10c).

3.2.3. Typhoon Contributions to the Dynamic and Thermal Changes of Eddies

The development and evolution of mesoscale eddies are influenced by a combination of factors, such as background flow, eddy interactions, topography, and wind stress. By performing numerical experiments (EXP-TC and EXP-NoTC), we can more accurately and quantitatively assess the contributions of typhoons to the growth of CEs. Here, SSH and EKE are selected as dynamic parameters; MLT and OHC are used as thermal parameters for the eddy response. The SSH, EKE, MLT, and OHC in the absence of typhoon influences, i.e., the EXP-TC simulation, can be considered background values, and the difference between the EXP-TC and EXP-NoTC simulations can be regarded as the contribution of Typhoon Surigae. Table 2 shows the SSH, EKE integrated above 200 m, MLT, and OHC of the eddy centers (C1: 126.5°E , 14.5°N ; C2: 124.5°E , 20°N) with and without typhoon effects. The SSH of C1 on 20 April was 0.979 m in the simulation without a typhoon and was lowered to 0.455 m on 20 April in the simulation with a typhoon. On 23 April, the SSH of C2 was 0.720 m in the simulation without a typhoon and 0.539 m in the simulation with a typhoon. Typhoon Surigae caused the SSH of C1 and C2 to lower by 53.52% and 25.14%, respectively, in comparison to the simulation without the typhoon. Typhoons also caused a 12-fold increase in the EKE for C1 and resulted in a 65.76% increase in the EKE for C2. There were

almost no significant changes in the MLT at the centers of C1 and C2 without the influence of the typhoon, while the MLT at the center of C1 decreased by 2.05 °C and that in the center of C2 decreased by 2.12 °C under typhoon conditions (Table 2). Typhoon Surigae caused the heat loss of the eddies. The OHC at the centers of C1 and C2 were reduced by 4000 MJ·m⁻² and 1178.7 MJ·m⁻², respectively, compared to the condition without the typhoon. The effect of the typhoon on the two CEs was not negligible.

Table 2. Variations in the SSH, EKE, mixed layer temperature (MLT) and ocean heat content (OHC) in EXP-TC and EXP-NoTC.

Eddy	Date (2021)	SSH (m)	EKE (m ³ ·s ⁻²)	MLT (°C)	OHC (×10 ⁴ MJ·m ⁻²)
C1 (EXP-TC)	17 April	1.062	3.942	28.217	2.10296
	20 April	0.455	39.690	26.218	1.70104
C1 (EXP-NoTC)	17 April	1.036	2.967	28.255	2.10250
	20 April	0.979	3.038	28.268	2.10104
C2 (EXP-TC)	20 April	0.678	13.773	25.933	1.78204
	23 April	0.539	20.172	24.890	1.67580
C2 (EXP-NoTC)	20 April	0.677	13.261	26.670	1.78993
	23 April	0.720	12.152	27.009	1.79367

3.3. Differences in the Responses of the Two CEs

3.3.1. EPV Response and PV Dynamics of CEs

The positive wind stress curl of Typhoon Surigae drove upwelling, and the EPV exceeded $5 \times 10^{-3} \text{ m}\cdot\text{s}^{-1}$ at C1 and $1.8 \times 10^{-3} \text{ m}\cdot\text{s}^{-1}$ at C2. During the interaction between the typhoon and C1, the typhoon moved more slowly and caused stronger upwelling (Figure 12a–c), and the typhoon passed through C2 relatively quickly and with a slightly weaker intensity, resulting in a smaller EPV than that of C1 (Figure 12d–f). This relatively strong pumping resulted in a greater perturbation of C1 and more significant dynamic adjustments (e.g., larger variations in the SSH).

Mesoscale eddies, as typical quasi-geostrophic motions, carry PV. During the relaxation stage after the passage of a typhoon, the geostrophic adjustment is essential for the upper ocean response [41]. Changes in the PV help us understand how the eddies evolve. Here, the PV anomaly is defined as the difference between the PV under typhoon conditions and the PV without typhoon forcing. After the typhoon passage, the isodensity line was uplifted, and a positive PV anomaly was found at a depth of 50–100 m in the center of the eddy; this anomaly propagated downward after the typhoon passage (Figure 13). The positive PV anomaly in the center of C1 was greater than that in C2, and the maximum PV anomaly in the center of C1 on 20 April was $3.01 \times 10^{-9} \text{ m}^{-1}\cdot\text{s}^{-1}$ (Figure 13b). The center of C2 exhibited negative PV anomalies in the mixed layer and positive PV anomalies at a depth of 100 m below the mixed layer (Figure 13f–h), indicating that the typhoon reduced the PV in the mixed layer and increased the PV in the thermocline. The background eddy has a positive PV, and a positive PVA represents a positive PV injection induced by the typhoon. Typhoons can inject positive oceanic PV anomalies through the geostrophic response and cause quasigeostrophic adjustment of the perturbed eddy [15]. According to this theory, the positive wind stress curl of Typhoon Surigae fed positive PV into the CEs, which perturbed the thermocline, and the unperturbed part partially adapted to the typhoon-induced changes in the thermocline, with the result that the CEs were dynamically enhanced.

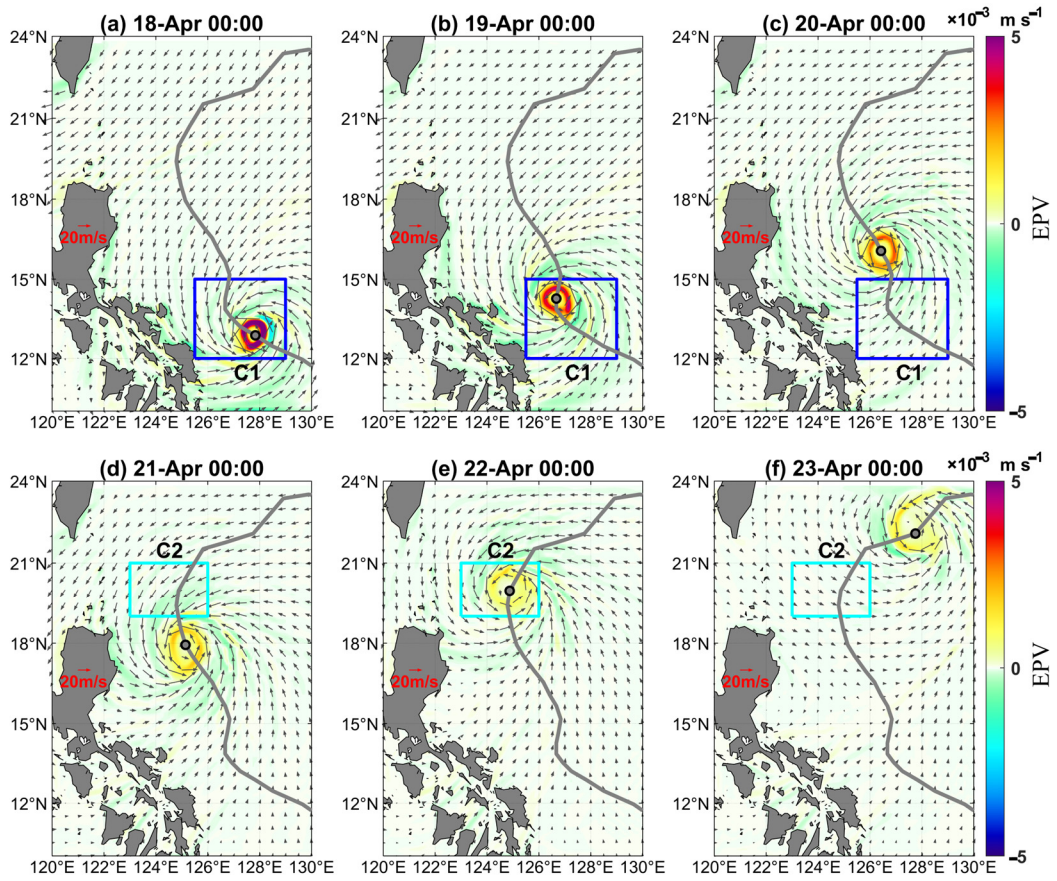


Figure 12. Wind speeds and Ekman pumping velocity (EPV) as Typhoon Surigae passed (a–c) C1 and (d–f) C2 simulated by EXP-TC. The gray arrows indicate 10 m wind vectors, the gray solid lines indicate typhoon tracks, and the dots are the typhoon positions at the corresponding times.

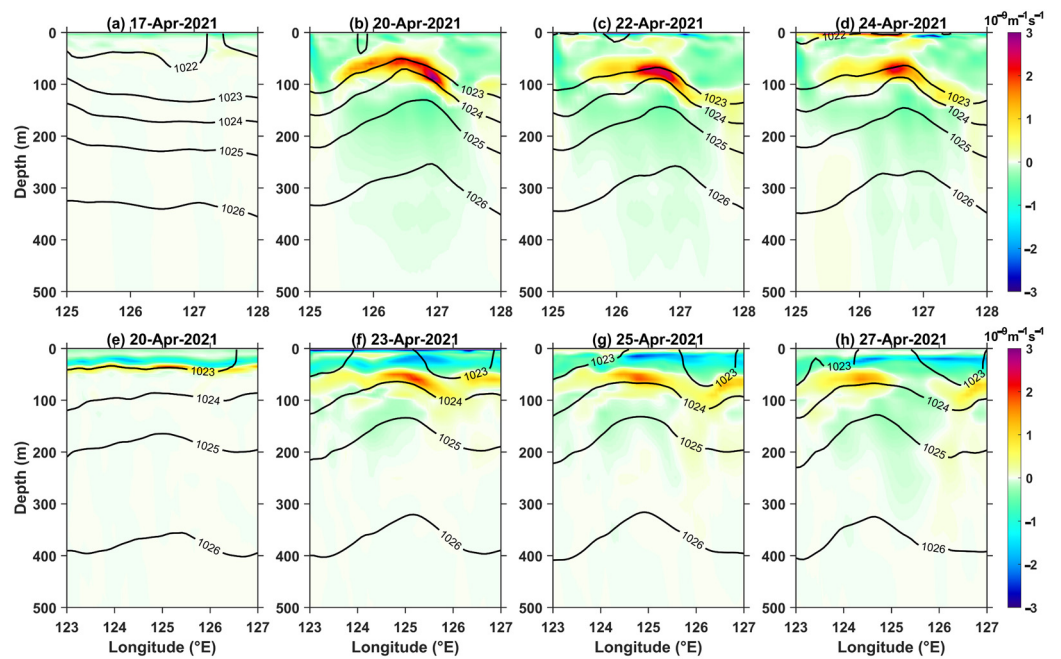


Figure 13. Vertical distributions of the potential vorticity (PV) anomalies in (a–d) C1 and (e–h) C2 before and after the typhoon. The locations of the sections are consistent with those in Figures 8a and 10a. The black solid lines indicate the contours of potential density ($\text{kg}\cdot\text{m}^{-3}$).

3.3.2. Temperature Response and Budget in CEs

To further understand the characteristics of the evolution of eddy temperature variation and the associated physical mechanisms, simulation results are used to calculate the mixed layer (ML) temperature budget. The ML temperature budget equation is given by [55]

$$\frac{\partial T}{\partial t} = -\left(u \frac{\partial T}{\partial x} + v \frac{\partial T}{\partial y} + w \frac{\partial T}{\partial z}\right) + \left(\frac{\partial}{\partial x} \left(A_h \frac{\partial T}{\partial x}\right) + \frac{\partial}{\partial y} \left(A_h \frac{\partial T}{\partial y}\right)\right) + \frac{\partial}{\partial z} \left(K_h \frac{\partial T}{\partial z}\right) + \frac{Q}{h\rho_0 C_p} \quad (12)$$

where $\frac{\partial T}{\partial t}$ is the temperature tendency term, which represents the rate of change in temperature with time ($^{\circ}\text{C}/\text{s}$); the first term on the right-hand side is the total advection, it is the sum of the horizontal advection and vertical advection. The second and third terms are horizontal and vertical diffusion, respectively. The fourth term is surface heat flux. In the diagnostic results output by COAWST, the surface heat flux term is included in the calculation of the vertical diffusion term [37].

After the passage of the typhoon, the center of C1 cooled rapidly, with the 27 $^{\circ}\text{C}$ isotherm outcropping (Figure 14a). For the surface layer temperature, the cooling of the temperature was dominated by vertical diffusion, and horizontal advection also contributed, but the total advection exhibited a warming effect on the SST due to the negative effect of vertical advection (Figure 14b). The temperature reduction at the bottom of the ML was mainly attributed to horizontal advection (Figure 14c). The cooling of the temperature at the center of C2 was lower (Figure 14d), and at the top of the ML, vertical diffusion first dominated the cooling process, after which the contribution of vertical advection increased (Figure 14e). As in C1, the temperature reduction at the bottom of the ML was mainly attributed to horizontal advection (Figure 14f). In the subsurface, the typhoon-induced enhancement of horizontal advection in the two CEs is the main mechanism of temperature cooling, whereas, on the surface, there was a difference in the physical mechanism of the variation in the temperature tendency between C1 and C2: for C1, it was mainly the typhoon-induced vertical entrainment mixing, whereas, for C2, vertical advection was more important in the modulation and enhancement of cooling.

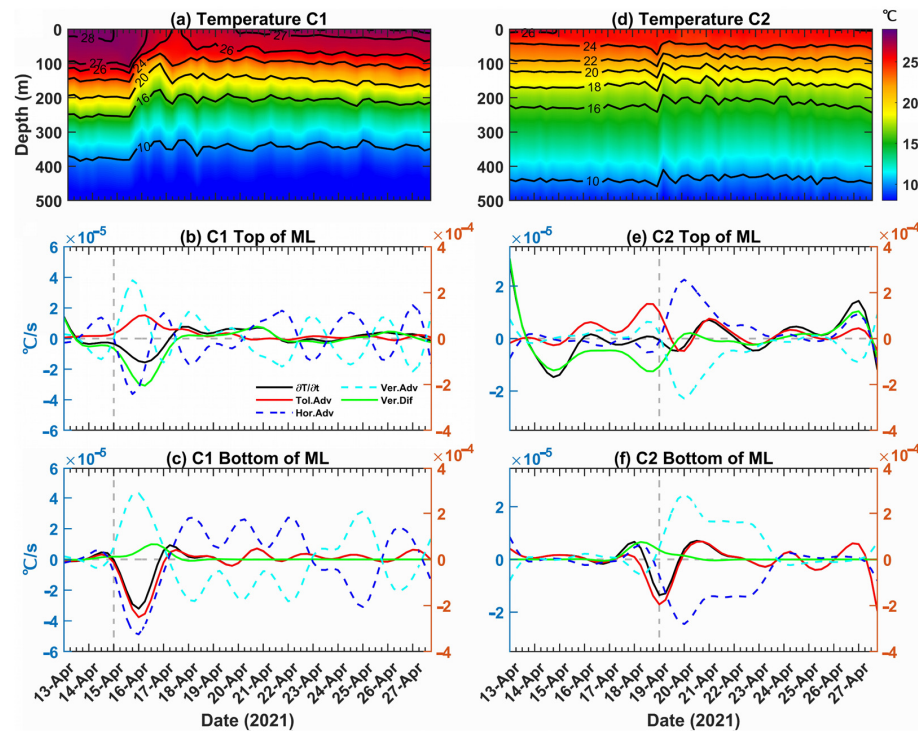


Figure 14. Temperature variations in the centers of (a) C1 and (d) C2 and the temporal evolution of the temperature tendency (black), total advection (red), horizontal advection (blue), vertical advection

(cyan) and vertical diffusion (green) in the mixed layer (ML) temperature budget at the top of the ML (2 m) of (b) C1 and (e) C2 and at the bottom of the ML (50 m) of (c) C1 and (f) C2. The terms in the temperature budget equation were low-pass filtered for 48 h using a Butterworth filter of third order. Note that in (b,c) and (e,f), the values of the terms represented by the solid lines are shown by the blue axis on the left, the terms represented by the dashed lines are shown by the red axis on the right, and the gray dashed lines represent the time the typhoon passed.

In summary, we found that there were differences in the responses of C1 and C2 to Typhoon Surigae, and in general, the typhoon had a stronger impact on C1 and contributed more to the development of the eddy during its lifetime. The differences in the responses of different eddies to typhoons are related to the track, typhoon intensity, and preconditions of the upper ocean [14].

In terms of the forcing time of Surigae, the forcing time of C1 (more than 70 h) was greater than that of C2 (Figure 15a). This is consistent with the larger EPV and PV adjustments of C1 (Figures 12 and 13), which can be attributed to the greater decrease in SSH and SST. The intensity of the typhoon was Category 4 and 5 when it passed through C1, which was greater than when it passed through C2 (Category 2 and 3), so the amount of work done on the C1 current was also greater than that on the C2 current. The maximum energy input on the right side of the typhoon track in C1 was $227.93 \text{ kJ}\cdot\text{m}^{-2}$, whereas the energy in the C2 region was less than $100 \text{ kJ}\cdot\text{m}^{-2}$ (Figure 15b). After the typhoon passed C1, a jet was generated, accompanied by an increase in the EKE.

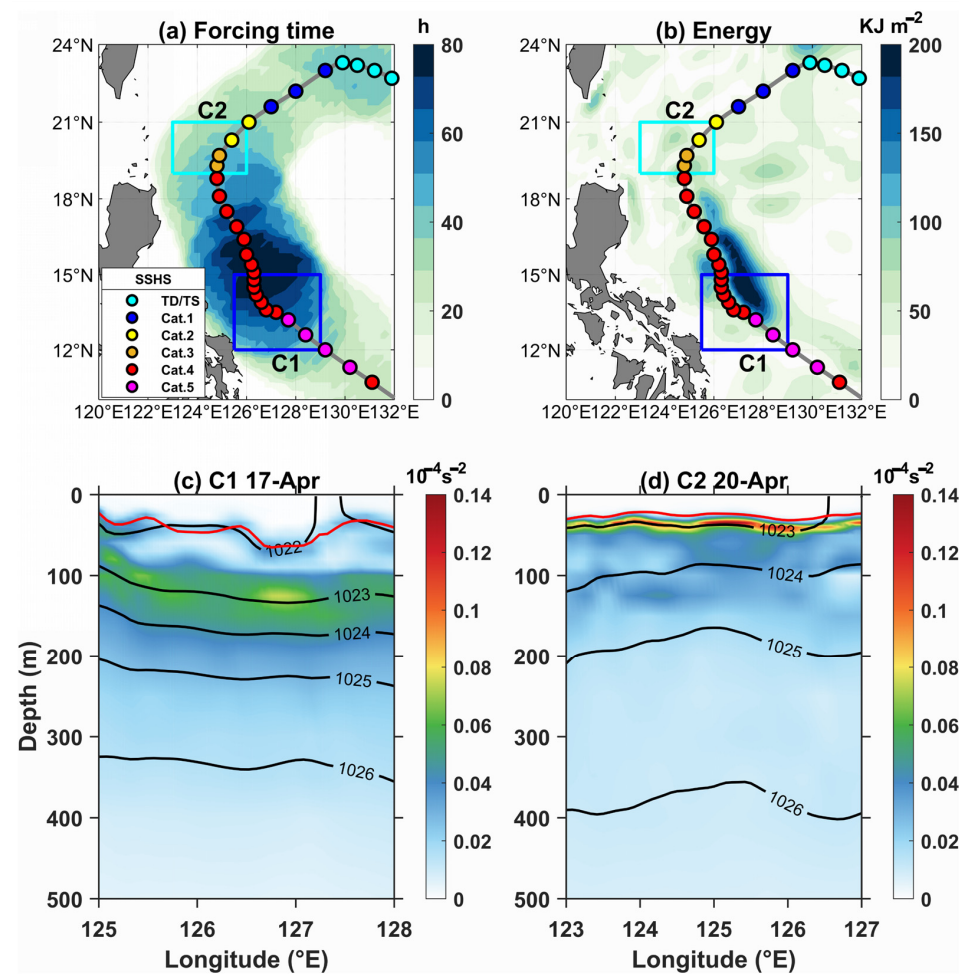


Figure 15. (a) Forcing time of Typhoon Surigae on the ocean; (b) energy input of Surigae to the ocean currents. In (a,b), the gray solid line indicates the track of Surigae, the colored dots represent the typhoon

intensity. Distribution of the buoyancy frequency N^2 in the cross-eddy sections (as in Figures 8a and 10a) on (c) 17 April before the typhoon's passage at C1 and (d) 20 April before the typhoon's passage at C2. The red solid lines indicate the mixed layer depth and the black solid lines denote the potential density contours ($\text{kg}\cdot\text{m}^{-3}$).

The strengths and thermal structures of mesoscale eddies differed before the typhoon passage. Dynamically, C1 was in the predevelopment stage before the typhoon, with insignificant upwelling, while C2 propagated from the east to the vicinity of the Luzon Strait before the typhoon's impact, with a strong eddy structure (Figures 2a and 3a). In terms of thermal structure, C1 had a deeper MLD and weaker stratification within the mixed layer, while C2 had strong vertical thermal stability due to stronger stratification below the mixed layer (Figure 15c,d). As a result, cold eddy C1, which had a weaker dynamic structure and an unstable thermal structure, rapidly strengthened and produced a stronger jet response. Moreover, due to the weaker cold core of C1 before the typhoon's impact, the heat content of C1 is higher, and more heat is lost after the passage of the typhoon than that of C2 (Table 2).

3.4. Impacts of CEs on the Kuroshio Current Associated with Surigae

Typhoon Surigae not only prolonged the lifetimes of C1 and C2 but also promoted the generation of a new cyclonic eddy (as previously discussed in Section 3.1.1. for the generated new eddy). Although the duration of the typhoon–eddy interaction was relatively brief, with the longest forcing time of the typhoon on the eddy being approximately three days (Figure 15a), the impact of the typhoon on the upper ocean was profound. This can be understood from the characteristics of the long-term evolution of eddies after the typhoon passes.

C1 was strengthened on 19 April (Figure 16a), then propagated westward to the Philippine coast (Figure 16b,c), and finally disappeared on 16 May (Figure 16d). C1 was active at the source of the Kuroshio, which may have had an impact on the Kuroshio downstream. The newly generated cyclonic eddy was first detected on 26 April (Figure 16e), then propagated northwestward (Figure 16f), interacted with the Kuroshio Current when it moved near 18°N , and finally merged into the Kuroshio Current and disappeared (Figure 16g,h). As a consequence of the convergence of the cyclonic eddy, the path of the Kuroshio shifted eastward at 18°N (Figure 16h). On 23 April, the center of C2 was located at 123.675°E , 19.875°N (Figure 16i), and then it proceeded to move westward with gradual weakening (Figure 16j,k). It was subsequently blocked by the Kuroshio and dissipated in the Luzon Strait (Figure 16l).

These three cyclonic eddies may have an impact on the Kuroshio Current according to their evolution, as shown in Figure 16, and we used the CMEMS reanalysis dataset to perform a preliminary analysis of the characteristics of the Kuroshio velocity in response to the eddies. Satellite altimeter data indicated that the surface Kuroshio velocity was reduced at three locations: 15°N , 18°N , and 21°N (Figure 17a,c). These correspond to the locations of C1, the new eddy, and C2 interactions with the Kuroshio, respectively. The reanalysis data are also consistent with the observations (Figure 17b,d). The 15°N section demonstrated a decrease in the maximum velocity at the core of the Kuroshio and a shift in the current axis to the west, which was related to C1 (Figure 17e–h). Prior to the influence of the typhoon and eddies, the magnitude of the velocity in the 18°N section exceeded $0.8\text{ m}\cdot\text{s}^{-1}$, with the core of the velocity located at 122.5°E (Figure 17f). Following the impact of the new cyclonic eddy, the velocity was less than $0.5\text{ m}\cdot\text{s}^{-1}$ at 122.5°E , while another core was identified near 124°E with a velocity exceeding $0.4\text{ m}\cdot\text{s}^{-1}$ (Figure 17i). Similarly, a reduction in the velocity was observed in the 21°N section, accompanied by a shift in the Kuroshio axis from 121°E to 120.5°E (Figure 17g,j).

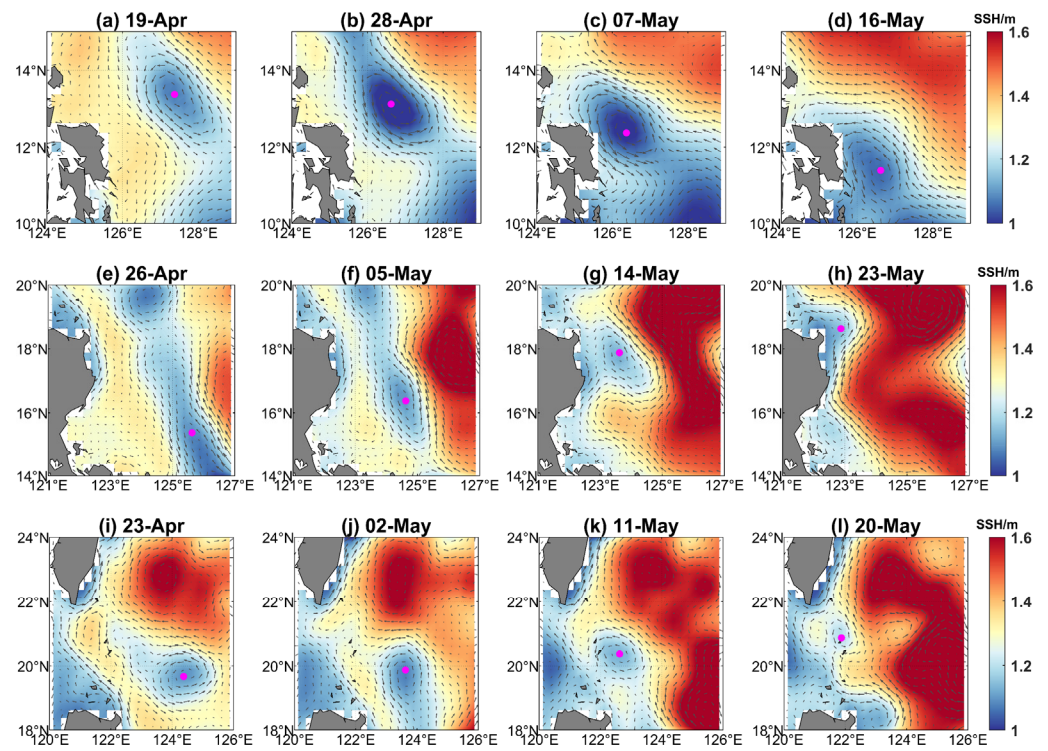


Figure 16. Spatial and temporal evolution of (a–d) C1, (e–h) new eddy, and (i–l) C2 based on SSH and geostrophic velocity. The magenta dots represent the eddy centers.

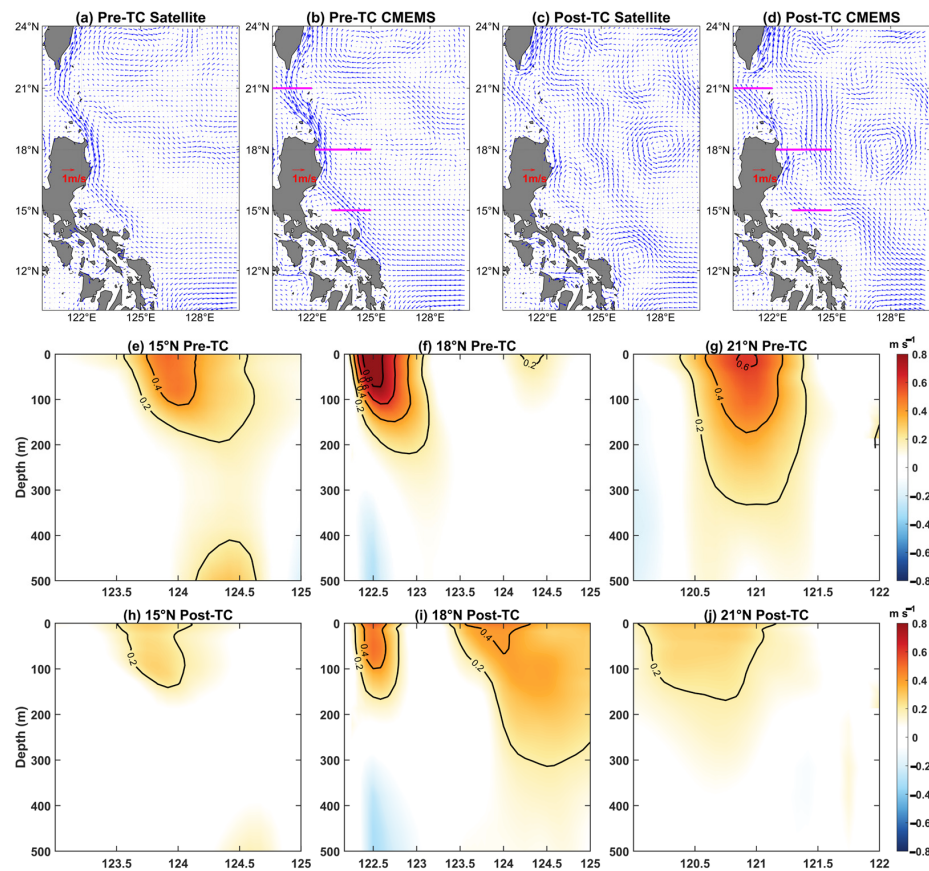


Figure 17. Distribution of (a) the surface geostrophic velocity based on satellite data and (b) the surface velocity based on the CMEMS in the pre-TC stage (averaged between 1 March and 18 April)

and (c,d) as in (a,b) but for the post-TC stage (averaged between 19 April and 25 May). Meridional velocity in sections (e) 15° N, (f) 18° N, and (g) 21° N (shown by solid magenta lines in (b,d)) in the pre-TC stage and (h–j) as in (e–g) but for the post-TC stage.

The volume transport of the Kuroshio Current was calculated by integrating the velocity above 500 m at the three sections indicated in Figure 17. The decreases in the Kuroshio transport were 60.33% at 15° N, 84.82% at 18° N, and 68.92% at 21° N after the typhoon (Figure 18a). In particular, Figure 18b shows that the Kuroshio transport in the spring of 2021 at 18° N (8.21 Sv) and 21° N (10.76 Sv) was the lowest over 30 years from 1993 to 2022. This indicates that the typhoon-related eddies that propagated to the western boundary current region and interacted with the Kuroshio in the spring resulted in a decrease in Kuroshio transport in the spring of 2021. In a sense, Typhoon Surigae influenced the seasonal features of the Kuroshio Current. The variation in the Kuroshio in this case study occurred on a short time scale (approximately one month), in contrast to the decadal variations in the Kuroshio east of Taiwan Island induced by TCs indicated by Zhang et al. [29].

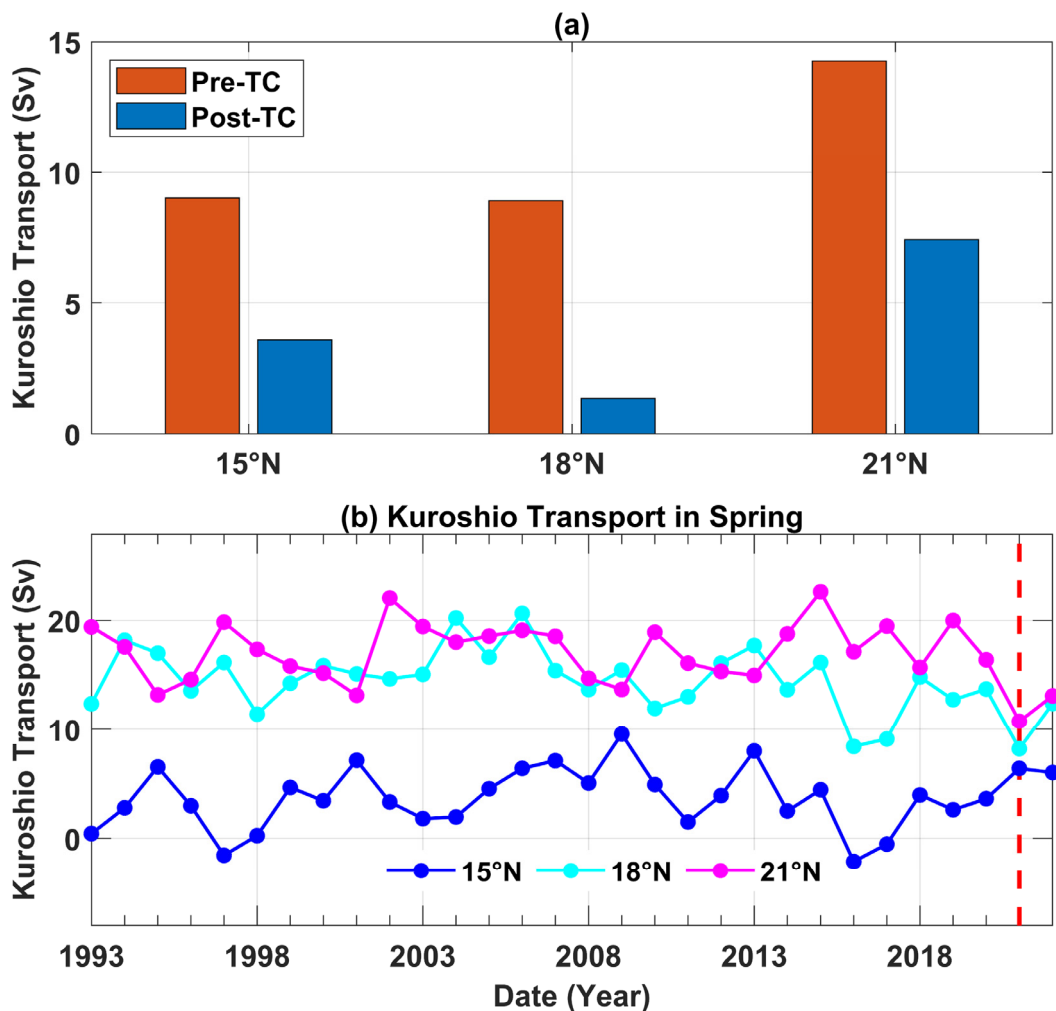


Figure 18. (a) Kuroshio transport in pre-TC and post-TC stages in three sections; (b) Kuroshio transport in spring (from March to May) from 1993 to 2022 in three sections. Sv: Sverdrup, 1Sv = 10⁶ m³/s. In (b), the vertical red dashed line represents 2021 in this case.

The results of the numerical simulations indicated that the development of CEs can be contingent upon typhoons (Figure 9). Therefore, typhoon perturbations in the upper ocean in the western boundary current region can affect the Kuroshio by creating oceanic

memory via mesoscale eddies. This finding is similar to that of a previous case in which typhoons affected the Kuroshio on northeastern Taiwan Island [56].

4. Conclusions

In this study, the surface and three-dimensional responses of two CEs in the WNPO forced by Typhoon Surigae were analyzed using observational data and a coupled ocean–atmosphere numerical model. The contributions of the typhoon to the EKE, SSH, and temperature changes in the eddies were also quantified via numerical comparative experiments. Additionally, the long-term evolution of eddies after typhoon perturbations and their impacts on the Kuroshio Current were preliminarily analyzed.

The results of both satellite data and coupled ocean–atmosphere model simulations consistently indicated that Typhoon Surigae had a significant impact on CEs in the western boundary current region of the WNPO. The typhoon passed the two preexisting CEs (C1 and C2), and both eddies strengthened, accompanied by the SSH trough under the typhoon track. Cyclonic eddy C1 exhibited elliptical stretching deformation under the influence of the typhoon, which resulted in the formation of jets on both sides of the typhoon track. The enhanced cold eddy modulated the typhoon-induced SST cooling, and the entrainment mixing and upwelling caused the temperature inside the eddy to decrease. The center of the eddy showed more significant SST cooling and propagated westward with the eddy. Previous studies that employed satellite or reanalysis data to quantify the impact of typhoons on the ocean normally utilized the variations that occurred before and after the typhoon’s passage. However, it is not possible to exclude the contribution of the evolution of the eddy itself, as well as the influence of background flow and other factors, to the change in the eddy. The results of the numerical comparison experiments demonstrated that the typhoon caused the SSHs of C1 and C2 to lower by 53.52% and 25.14% relative to the simulation without typhoon, respectively. Additionally, the EKE increased by a factor of 12 and 65.76%, respectively. Furthermore, the mixed-layer temperatures decreased by 2.05 °C and 2.12 °C, respectively. The heat content at the centers of C1 and C2 lost 4000 MJ·m⁻² and 1178.7 MJ·m⁻², respectively, compared to the case without the typhoon.

A positive anomaly in the PV input from the typhoon to the upper ocean was the primary cause of eddy enhancement. Due to the differing intensity of the typhoon as it passed the two CEs and the differences in the preconditions of the two CEs before the typhoon passed, the responses of the two CEs differed after PV adjustment. On the one hand, the typhoon forcing time of C1 was longer, resulting in a more pronounced EPV and a greater perturbation of C1. A relatively strong pumping effect also resulted in the SSH being greatly lowered. Furthermore, the work done by the typhoon on the currents of C1 was greater than that on C2, leading to stronger jets and EKE and a more drastic deformation of C1. Conversely, prior to the typhoon, C1 was a cold eddy with a weaker dynamic structure and an unstable thermal structure compared to C2. Consequently, C1 rapidly intensified and produced a more intense temperature decrease under the influence of the super typhoon Surigae. The SST cooling of C1 was dominated by typhoon-induced vertical entrainment mixing, while vertical advection was the primary regulator of SST cooling in C2.

Furthermore, our study revealed that typhoons can significantly alter the eddy field by strengthening and generating cyclonic eddies and weakening anticyclonic eddies, which in turn affects the large-scale circulation along the western boundary. In the month following the typhoon’s passage, two CEs enhanced by the typhoon and one cyclonic eddy generated by the typhoon perturbation propagated westward to interact with the Kuroshio. The transport of Kuroshio Current in three sections decreased by 60.33%, 84.82%, and 68.92%, respectively, as a result of the influence of cyclonic eddies. The new cyclonic eddy and C2 probably caused the Kuroshio Current transport at 18° N and 21° N in the spring of 2021 to be the lowest in the last 30 years.

This study emphasizes the direct impacts of typhoons on oceanic cyclonic eddies and their remote effects on the Kuroshio Current and provides evidence that typhoons

influence large-scale circulation via mesoscale eddies. The findings from this case contribute to a deeper understanding of the typhoon–eddy interactions and will help further improve TC forecasting. Considering that many mesoscale eddies move from the east to the Kuroshio in the Luzon Strait and east of Luzon Island and are likely to be affected by typhoons during their movement, our study provides a reference for further analyzing the response mechanism of eddies to typhoons in this region and the impact of typhoons on the Kuroshio Current. However, the cumulative effect of more frequent typhoons on large-scale circulation, such as the Kuroshio near the Luzon Strait, under a changing climate remains uncertain. The typhoon–eddy–Kuroshio interaction needs to be further investigated by combining numerical models with in situ observations in additional cases.

Supplementary Materials: The following supporting information can be downloaded at: <https://www.mdpi.com/article/10.3390/jmse12071202/s1>, Table S1: Observation of mooring M1; Figure S1: Variation in the wind stress curl simulated by (a–d) COAWST EXP-TC under typhoon conditions and (e–h) COAWST EXP-NoTC without a typhoon.

Author Contributions: Conceptualization, S.H. and Y.Z.; methodology, S.H. and Y.Z.; validation, Y.Z.; formal analysis, Y.Z.; investigation, Y.Z.; resources, S.H. and Y.Z.; data curation, Y.Z.; writing—original draft preparation, Y.Z.; writing—review and editing, S.H.; visualization, Y.Z.; supervision, S.H.; project administration, S.H.; funding acquisition, S.H. All authors have read and agreed to the published version of the manuscript.

Funding: This research was funded by the National Key Research and Development Program of China (Grant No. 2022YFC3104000) and the Innovation Research Project for Marine Science and Technology of Jiangsu Province (Grant No. JSZRHYKJ202304).

Institutional Review Board Statement: Not applicable.

Informed Consent Statement: Not applicable.

Data Availability Statement: The IBTrACS typhoon data were obtained from the NOAA (<https://www.ncdc.noaa.gov/ibtracs/index.php?name=ib-v4-access>, accessed on 6 December 2023). The typhoon tracks data were acquired from the CMA (<https://tcdata.typhoon.org.cn/zjljsjj.html>, accessed on 6 December 2023) and JMA (<https://www.jma.go.jp/jma/jma-eng/jma-center/rsmc-hp-pub-eg/besttrack.html>, accessed on 6 December 2023). The SLA, SSH, geostrophic velocity, and SST data were provided by the CMEMS (<https://data.marine.copernicus.eu/products>, accessed on 1 December 2023). The CMEMS ocean reanalysis datasets were downloaded from <https://data.marine.copernicus.eu/products> (accessed on 13 May 2024). The CCMP data were downloaded from <http://www.remss.com> (accessed on 21 November 2023). The Argo float data were downloaded from <https://fleetmonitoring.euro-argo.eu/> (accessed on 14 April 2024). The HYCOM reanalysis data and NCEP FNL analysis data were available from <https://www.hycom.org/> (accessed on 15 January 2024) and <https://rda.ucar.edu/datasets/ds083.2/> (accessed on 15 January 2024), respectively. Data from the coupled model and mooring observations will be made available on request from the corresponding author.

Acknowledgments: We sincerely thank the anonymous reviewers and editors for their valuable comments and suggestions that improved this paper. We appreciate the institutions or organizations mentioned in the Data Availability Statement.

Conflicts of Interest: The authors declare no conflicts of interest.

References

1. Price, J.F. Upper Ocean Response to a Hurricane. *J. Phys. Oceanogr.* **1981**, *11*, 153–175. [[CrossRef](#)]
2. Price, J.F.; Sanford, T.B.; Forristall, G.Z. Forced stage response of moving hurricane. *J. Phys. Oceanogr.* **1994**, *24*, 233–260. [[CrossRef](#)]
3. Emanuel, K. Contribution of tropical cyclones to meridional heat transport by the oceans. *J. Geophys. Res. Atmos.* **2001**, *106*, 14771–14781. [[CrossRef](#)]
4. Lin, I.I.; Liu, W.T.; Wu, C.; Chiang, J.C.H.; Sui, C. Satellite observations of modulation of surface winds by typhoon-induced upper ocean cooling. *Geophys. Res. Lett.* **2003**, *30*, 1131. [[CrossRef](#)]
5. Zhang, H.; He, H.; Zhang, W.; Tian, D. Upper ocean response to tropical cyclones: A review. *Geosci. Lett.* **2021**, *8*, 1. [[CrossRef](#)]
6. Chelton, D.B.; Schlax, M.G.; Samelson, R.M. Global observations of nonlinear mesoscale eddies. *Prog. Oceanogr.* **2011**, *91*, 167–216. [[CrossRef](#)]

7. Zhang, Z.; Wang, W.; Qiu, B. Oceanic mass transport by mesoscale eddies. *Science* **2014**, *345*, 322–324. [[CrossRef](#)] [[PubMed](#)]
8. Lien, R.; Ma, B.; Cheng, Y.; Ho, C.; Qiu, B.; Lee, C.M.; Chang, M. Modulation of Kuroshio transport by mesoscale eddies at the Luzon Strait entrance. *J. Geophys. Res. Ocean.* **2014**, *119*, 2129–2142. [[CrossRef](#)]
9. Dong, D.; Brandt, P.; Chang, P.; Schütte, F.; Yang, X.; Yan, J.; Zeng, J. Mesoscale Eddies in the Northwestern Pacific Ocean: Three-Dimensional Eddy Structures and Heat/Salt Transports. *J. Geophys. Res. Ocean.* **2017**, *122*, 9795–9813. [[CrossRef](#)]
10. Liu, S.; Sun, L.; Wu, Q.; Yang, Y. The responses of cyclonic and anticyclonic eddies to typhoon forcing: The vertical temperature-salinity structure changes associated with the horizontal convergence/divergence. *J. Geophys. Res. Ocean.* **2017**, *122*, 4974–4989. [[CrossRef](#)]
11. Wang, G.; Wu, L.; Mei, W.; Xie, S. Ocean currents show global intensification of weak tropical cyclones. *Nature* **2022**, *611*, 496–500. [[CrossRef](#)]
12. Wang, H.; Wang, C. What caused the increase of tropical cyclones in the western North Pacific during the period of 2011–2020? *Clim. Dyn.* **2023**, *60*, 165–177. [[CrossRef](#)]
13. Ma, Z.; Fei, J.; Liu, L.; Huang, X.; Li, Y. An Investigation of the Influences of Mesoscale Ocean Eddies on Tropical Cyclone Intensities. *Mon. Weather Rev.* **2017**, *145*, 1181–1201. [[CrossRef](#)]
14. Yu, F.; Yang, Q.; Chen, G.; Li, Q. The response of cyclonic eddies to typhoons based on satellite remote sensing data for 2001–2014 from the South China Sea. *Oceanologia* **2019**, *61*, 265–275. [[CrossRef](#)]
15. Lu, Z.; Wang, G.; Shang, X. Response of a Preexisting Cyclonic Ocean Eddy to a Typhoon. *J. Phys. Oceanogr.* **2016**, *46*, 2403–2410. [[CrossRef](#)]
16. Sun, L.; Li, Y.; Yang, Y.; Wu, Q.; Chen, X.; Li, Q.; Li, Y.; Xian, T. Effects of super typhoons on cyclonic ocean eddies in the western North Pacific: A satellite data-based evaluation between 2000 and 2008. *J. Geophys. Res. Ocean.* **2014**, *119*, 5585–5598. [[CrossRef](#)]
17. Shang, X.; Zhu, H.; Chen, G.; Xu, C.; Yang, Q. Research on Cold Core Eddy Change and Phytoplankton Bloom Induced by Typhoons: Case Studies in the South China Sea. *Adv. Meteorol.* **2015**, *2015*, 1–19. [[CrossRef](#)]
18. Hu, J.; Kawamura, H. Detection of cyclonic eddy generated by looping tropical cyclone in the northern South China Sea: A case study. *Acta Oceanol. Sin.* **2004**, *23*, 213–224.
19. Shen, Z.; Zhang, S. The generation mechanism of cold eddies and the related heat flux exchanges in the upper ocean during two sequential tropical cyclones. *Front. Mar. Sci.* **2022**, *9*, 1061159. [[CrossRef](#)]
20. Walker, N.D.; Leben, R.R.; Balasubramanian, S. Hurricane-forced upwelling and chlorophylla enhancement within cold-core cyclones in the Gulf of Mexico. *Geophys. Res. Lett.* **2005**, *32*, L18610. [[CrossRef](#)]
21. Zheng, Z.; Ho, C.; Kuo, N. Importance of pre-existing oceanic conditions to upper ocean response induced by Super Typhoon Hai-Tang. *Geophys. Res. Lett.* **2008**, *35*, L20603. [[CrossRef](#)]
22. Zheng, Z.; Ho, C.; Zheng, Q.; Lo, Y.; Kuo, N.; Gopalakrishnan, G. Effects of preexisting cyclonic eddies on upper ocean responses to Category 5 typhoons in the western North Pacific. *J. Geophys. Res.* **2010**, *115*, C9013. [[CrossRef](#)]
23. Jaimes, B.; Shay, L.K. Enhanced Wind-Driven Downwelling Flow in Warm Oceanic Eddy Features during the Intensification of Tropical Cyclone Isaac (2012): Observations and Theory. *J. Phys. Oceanogr.* **2015**, *45*, 1667–1689. [[CrossRef](#)]
24. Ma, Z.; Fei, J.; Huang, X.; Cheng, X. Modulating Effects of Mesoscale Oceanic Eddies on Sea Surface Temperature Response to Tropical Cyclones Over the Western North Pacific. *J. Geophys. Res. Atmos.* **2018**, *123*, 367–379. [[CrossRef](#)]
25. Jaimes, B.; Shay, L.K. Near-Inertial Wave Wake of Hurricanes Katrina and Rita over Mesoscale Oceanic Eddies. *J. Phys. Oceanogr.* **2010**, *40*, 1320–1337. [[CrossRef](#)]
26. Jaimes, B.; Shay, L.K.; Halliwell, G.R. The Response of Quasigeostrophic Oceanic Vortices to Tropical Cyclone Forcing. *J. Phys. Oceanogr.* **2011**, *41*, 1965–1985. [[CrossRef](#)]
27. Li, X.; Cheng, X.; Fei, J.; Huang, X. A Numerical Study on the Role of Mesoscale Cold-Core Eddies in Modulating the Upper-Ocean Responses to Typhoon Trami (2018). *J. Phys. Oceanogr.* **2022**, *52*, 3101–3122. [[CrossRef](#)]
28. Zhang, Z.; Zheng, Y.; Li, H. Imprints of tropical cyclone on three-dimensional structural characteristics of mesoscale oceanic eddies. *Front. Earth Sci.* **2023**, *10*, 1057798. [[CrossRef](#)]
29. Zhang, Y.; Zhang, Z.; Chen, D.; Qiu, B.; Wang, W. Strengthening of the Kuroshio current by intensifying tropical cyclones. *Science* **2020**, *368*, 988–993. [[CrossRef](#)]
30. Lu, Z.; Wang, G.; Shang, X. Observable Large-Scale Impacts of Tropical Cyclones on the Subtropical Gyre. *J. Phys. Oceanogr.* **2023**, *53*, 2189–2209. [[CrossRef](#)]
31. Wada, A. Roles of Oceanic Mesoscale Eddy in Rapid Weakening of Typhoons Trami and Kong-Rey in 2018 Simulated with a 2-km-Mesh Atmosphere-Wave-Ocean Coupled Model. *J. Meteorol. Soc. Jpn. Ser. II* **2021**, *99*, 1453–1482. [[CrossRef](#)]
32. Li, X.; Cheng, X.; Fei, J.; Huang, X.; Ding, J. The modulation effect of sea surface cooling on the eyewall replacement cycle in Typhoon Trami (2018). *Mon. Weather Rev.* **2022**, *150*, 1417–1436. [[CrossRef](#)]
33. Webster, P.J.; Holland, G.J.; Curry, J.A.; Chang, H.R. Changes in Tropical Cyclone Number, Duration, and Intensity in a Warming Environment. *Science* **2005**, *309*, 1844–1846. [[CrossRef](#)]
34. Levinson, D.H.; Diamond, H.J. Combining Tropical Cyclone Data Sets Worldwide: International Best Track Archive for Climate Stewardship (IBTrACS) Workshop; Asheville, North Carolina, 5–7 May 2009. *Eos Trans. Am. Geophys. Union* **2009**, *90*, 301. [[CrossRef](#)]
35. Wu, R.; Li, C. Upper ocean response to the passage of two sequential typhoons. *Deep. Sea Res. Part I Oceanogr. Res. Pap.* **2018**, *132*, 68–79. [[CrossRef](#)]

36. Li, J.; Zhang, H.; Liu, S.; Wang, X.; Sun, L. The Response and Feedback of Ocean Mesoscale Eddies to Four Sequential Typhoons in 2014 Based on Multiple Satellite Observations and Argo Floats. *Remote Sens.* **2021**, *13*, 3805. [[CrossRef](#)]
37. Lin, S.; Zhang, W.; Wang, Y.; Chai, F. Mechanism of oceanic eddies in modulating the sea surface temperature response to a strong typhoon in the western North Pacific. *Front. Mar. Sci.* **2023**, *10*, 1117301. [[CrossRef](#)]
38. Donlon, C.J.; Martin, M.; Stark, J.; Roberts-Jones, J.; Fiedler, E.; Wimmer, W. The Operational Sea Surface Temperature and Sea Ice Analysis (OSTIA) system. *Remote Sens. Environ.* **2012**, *116*, 140–158. [[CrossRef](#)]
39. Mears, C.A.; Scott, J.; Wentz, F.J.; Ricciardulli, L.; Leidner, S.M.; Hoffman, R.; Atlas, R. A Near-Real-Time Version of the Cross-Calibrated Multiplatform (CCMP) Ocean Surface Wind Velocity Data Set. *J. Geophys. Res. Ocean.* **2019**, *124*, 6997–7010. [[CrossRef](#)]
40. Powell, M.D.; Vickery, P.J.; Reinhold, T.A. Reduced drag coefficient for high wind speeds in tropical cyclones. *Nature* **2003**, *422*, 279–283. [[CrossRef](#)] [[PubMed](#)]
41. Lu, Z.; Wang, G.; Shang, X. Strength and Spatial Structure of the Perturbation Induced by a Tropical Cyclone to the Underlying Eddies. *J. Geophys. Res. Ocean.* **2020**, *125*, e2020JC016097. [[CrossRef](#)]
42. Sadarjoen, I.A.; Post, F.H. Detection, quantification, and tracking of vortices using streamline geometry. *Comput. Graph.* **2000**, *24*, 333–341. [[CrossRef](#)]
43. Chaigneau, A.; Gizolme, A.; Grados, C. Mesoscale eddies off Peru in altimeter records: Identification algorithms and eddy spatio-temporal patterns. *Prog. Oceanogr.* **2008**, *79*, 106–119. [[CrossRef](#)]
44. Zedler, S.E.; Dickey, T.D.; Doney, S.C.; Price, J.F.; Yu, X.; Mellor, G.L. Analyses and simulations of the upper ocean's response to Hurricane Felix at the Bermuda Testbed Mooring site: 13–23 August 1995. *J. Geophys. Res. Ocean.* **2002**, *107*, 21–25. [[CrossRef](#)]
45. Warner, J.C.; Armstrong, B.; He, R.; Zambon, J.B. Development of a Coupled Ocean–Atmosphere–Wave–Sediment Transport (COAWST) Modeling System. *Ocean Model.* **2010**, *35*, 230–244. [[CrossRef](#)]
46. Kain, J.S. The Kain–Fritsch Convective Parameterization: An Update. *J. Appl. Meteorol.* **2004**, *43*, 170–181. [[CrossRef](#)]
47. Chen, S.; Sun, W. A One-dimensional Time Dependent Cloud Model. *J. Meteorol. Soc. Jpn. Ser. II* **2002**, *80*, 99–118. [[CrossRef](#)]
48. Hong, S.; Noh, Y.; Dudhia, J. A New Vertical Diffusion Package with an Explicit Treatment of Entrainment Processes. *Mon. Weather Rev.* **2006**, *134*, 2318–2341. [[CrossRef](#)]
49. Tewari, M.; Chen, F.; Wang, W.; Dudhia, J.; Lemone, A.; Mitchell, E.; Ek, M.B.; Gayno, G.; Węgiel, W.; Cuenca, R.H. Implementation and verification of the unified Noah land-surface model in the WRF model. In Proceedings of the 20th Conference on Weather Analysis and Forecasting/16th Conference on Numerical Weather Prediction, Seattle, WA, USA, 12–16 January 2004; Volume 14, pp. 11–15.
50. Dudhia, J. Numerical Study of Convection Observed during the Winter Monsoon Experiment Using a Mesoscale Two-Dimensional Model. *J. Atmos. Sci.* **1989**, *46*, 3077–3107. [[CrossRef](#)]
51. Mlawer, E.J.; Taubman, S.J.; Brown, P.D.; Iacono, M.J.; Clough, S.A. Radiative transfer for inhomogeneous atmospheres: RRTM, a validated correlated-k model for the longwave. *J. Geophys. Res. Atmos.* **1997**, *102*, 16663–16682. [[CrossRef](#)]
52. Li, J.; Sun, L.; Yang, Y.; Cheng, H. Accurate Evaluation of Sea Surface Temperature Cooling Induced by Typhoons Based on Satellite Remote Sensing Observations. *Water* **2020**, *12*, 1413. [[CrossRef](#)]
53. De Boyer Montégut, C.; Madec, G.; Fischer, A.S.; Lazar, A.; Iudicone, D. Mixed layer depth over the global ocean: An examination of profile data and a profile-based climatology. *J. Geophys. Res. Ocean.* **2004**, *109*, C12003. [[CrossRef](#)]
54. Rudzin, J.E.; Chen, S. On the dynamics of the eradication of a warm core mesoscale eddy after the passage of Hurricane Irma (2017). *Dyn. Atmos. Oceans.* **2022**, *100*, 101334. [[CrossRef](#)]
55. Wei, J.; Liu, X.; Wang, D.X. Dynamic and thermal responses of the Kuroshio to typhoon Megi (2004). *Geophys. Res. Lett.* **2014**, *41*, 8495–8502. [[CrossRef](#)]
56. Jeon, C.; Watts, D.R.; Min, H.S.; Kim, D.G.; Kang, S.K.; Moon, I.; Park, J. Weakening of the Kuroshio Upstream by Cyclonic Cold Eddies Enhanced by the Consecutive Passages of Typhoons Danas, Wipha, and Francisco (2013). *Front. Mar. Sci.* **2022**, *9*, 884768. [[CrossRef](#)]

Disclaimer/Publisher's Note: The statements, opinions and data contained in all publications are solely those of the individual author(s) and contributor(s) and not of MDPI and/or the editor(s). MDPI and/or the editor(s) disclaim responsibility for any injury to people or property resulting from any ideas, methods, instructions or products referred to in the content.